

## 1                    **Goblet Cell Hyperplasia Increases SARS-CoV-2 Infection in COPD.**

2                    Jaspreet K. Osan<sup>1,4</sup>, Sattya N. Talukdar<sup>1,4</sup>, Friederike Feldmann<sup>2</sup>, Beth Ann DeMontigny<sup>1</sup>,

3                    Kailey Jerome<sup>1</sup>, Kristina L. Bailey<sup>3</sup>, Heinz Feldmann<sup>2</sup>, and Masfique Mehedi<sup>1,5,\*</sup>

4                    <sup>1</sup>Department of Biomedical Sciences, University of North Dakota School of Medicine & Health  
5                    Sciences, Grand Forks, ND 58202, USA.

6                    <sup>2</sup>Divison of Intramural Research, Rocky Mountain Laboratories, National Institute of Allergy  
7                    and Infectious Diseases, National Institutes of Health, Hamilton, MT 59840, USA.

8                    <sup>3</sup>Department of Internal Medicine, Pulmonary, Critical Care and Sleep and Allergy, University  
9                    of Nebraska Medical Center, Omaha, NE 68198, USA.

10                    <sup>4</sup>Contributed equally to this study

11                    <sup>5</sup>Lead contact

12                    \*Correspondence: [masfique.mehedi@und.edu](mailto:masfique.mehedi@und.edu)

13  
14                    **Summary.** SARS-CoV-2 has become a major problem across the globe, with approximately 50  
15                    million cases and more than 1 million deaths and currently no approved treatment or vaccine.  
16                    Chronic obstructive pulmonary disease (COPD) is one of the underlying conditions in adults of  
17                    any age that place them at risk for developing severe illness associated with COVID-19. We  
18                    established an airway epithelium model to study SARS-CoV-2 infection in healthy and COPD  
19                    lung cells. We found that both the entry receptor ACE2 and the co-factor transmembrane  
20                    protease TMPRSS2 are expressed at higher levels on nonciliated goblet cell, a novel target for  
21                    SARS-CoV-2 infection. We observed that SARS-CoV-2 infected goblet cells and induced  
22                    syncytium formation and cell sloughing. We also found that SARS-CoV-2 replication was

23 increased in the COPD airway epithelium likely due to COPD associated goblet cell hyperplasia.  
24 Our results reveal goblet cells play a critical role in SARS-CoV-2 infection in the lung.

25

26 **Keywords.** SARS-CoV-2, COVID-19, goblet cells, ciliated cells, COPD, squamous metaplasia,  
27 air-liquid interface, syncytium, cell sloughing, goblet cell hyperplasia.

28

29 **Introduction.** Severe acute respiratory syndrome coronavirus 2 (SARS-CoV-2, a causative agent  
30 of coronavirus disease 2019, COVID-19) that emerged in December 2019 in Wuhan, China.  
31 Since then, this pathogen has caused havoc in the healthcare systems worldwide and  
32 consequentially ravaged the economy of countries with COVID-19 outbreaks. There is currently  
33 no FDA-approved vaccine against SARS-CoV-2. SARS-CoV-2 is a nonsegmented, positive-  
34 sense, single-strand RNA virus that causes both upper and lower respiratory tract infections.  
35 Most patients exhibit fever and cough, and a subset of patients advance to severe acute  
36 respiratory distress syndrome (ARDS) (Guan et al., 2020; Yang et al., 2020). Therefore, patients  
37 with underlying chronic obstructive pulmonary disease (COPD) are vulnerable to COVID-19,  
38 and in fact, COPD is one of the high-risk factors for severe illness associated with COVID-19  
39 (CDC, 2020; Leung et al., 2020; Sin, 2020).

40 Viral infections begin by the attachment of viral particles to entry receptors on the host  
41 cell. The tissue expression and distribution of the SARS-CoV-2 entry receptor angiotensin-  
42 converting enzyme 2 (ACE2) and its co-factor transmembrane serine protease 2 (TMPRSS2)  
43 determine the tropism of virus infection (Hoffmann et al., 2020; Li et al., 2003), and viral  
44 infection in human airway epithelium depends on ACE2 expression (Hamming et al., 2004; Jia et  
45 al., 2006). For successful entry into cells, SARS-CoV-2 uses the serine protease TMPRSS2 for S

46 protein priming (Hoffmann et al., 2020). ACE2 is highly expressed in the small intestine, testis,  
47 kidneys, heart, thyroid, and adipose tissue and is expressed at moderate expression levels in the  
48 lung, colon, liver, bladder, and adrenal gland; and lowest in the blood, spleen, bone marrow,  
49 brain, blood vessels, and muscle (Hamming et al., 2004; Li et al., 2020). ACE2 expression in the  
50 lungs is predominantly observed in alveolar type 2 (AT2) cells (Lukassen et al., 2020; Qi et al.,  
51 2020; To and Lo, 2004; Ziegler et al., 2020), but ciliated cells also express ACE2 in the  
52 respiratory epithelium (Sims et al., 2005). Recent RNAseq-based studies have suggested that  
53 ACE2 is more highly expressed on goblet cells in the nasal airways and on secretory cells in  
54 subsegmental bronchial branches of the lung (Lukassen et al., 2020; Sungnak et al., 2020;  
55 Ziegler et al., 2020). Although ACE2 and TMPRSS2 expressions are higher in nonciliated goblet  
56 cells compared to ciliated cells (Lukassen et al., 2020; Sungnak et al., 2020; Zhang et al., 2020;  
57 Ziegler et al., 2020), it appears that goblet cells are underappreciated in the SARS-CoV-2  
58 infection studies. The possibility that SARS-CoV-2 infects goblet cells could explain the  
59 presence of viral RNA in sputum (Wang et al., 2020) and might explain the efficient  
60 transmission of the virus from person to person (Dhand and Li, 2020; Wolfel et al., 2020).  
61 Importantly, goblet cell hyperplasia is a characteristic pathological feature of COPD patients,  
62 who are vulnerable to severe disease associated with COVID-19 (Lippi and Henry, 2020;  
63 Shimura et al., 1996; Zhao et al., 2020). Therefore, it is prudent to determine to what extent  
64 SARS-CoV-2 infects goblet cells in the lung.

65 To determine the expression of the SARS-CoV-2 receptor and its preferential cell tropism  
66 in the lung, we developed an in vitro airway epithelium model by differentiating primary normal  
67 human bronchial (NHBE) cells derived from either a patient with COPD or a healthy adult (non-  
68 COPD). The COPD airway epithelium model recapitulates many bronchial characteristics of

69 COPD. We evaluated the expression of ACE2 and TMPRSS2 and studied SARS-CoV-2  
70 infection in these in vitro airway epithelium models. We found that SARS-CoV-2 primarily  
71 infects nonciliated goblet cells due to high expression of both ACE2 and TMPRSS2 in these  
72 cells. Goblet cell hyperplasia increases of SARS-CoV-2 infection in the COPD airway  
73 epithelium. Thus, SARS-CoV-2 targeting and replication in goblet cells may explain the  
74 development of more severe COVID-19 in COPD patients.

75

## 76 **Results.**

### 77 **The airway epithelium model recapitulates the chronic bronchial characteristics of COPD.**

78 We first established an in vitro airway epithelium model by differentiating NHBE cells from  
79 either a healthy adult or a COPD patient (deidentified) at the air-liquid interface (ALI). We found  
80 that 4 weeks of differentiation provides a fully differentiated pseudostratified mucociliary airway  
81 epithelium for both conditions (Figures 1A and B), which allows the use of this model for side-  
82 by-side comparisons. NHBE cells from a healthy adult differentiated primarily into a  
83 pseudostratified columnar epithelium, whereas the NHBE cells from a COPD patient  
84 differentiated into a mix of pseudostratified and stratified columnar epithelium that contained all  
85 three main cell types of the respiratory epithelium (Pawlina, 2016; Rayner et al., 2019; Rigden et  
86 al., 2016): ciliated cells, goblet cells, and basal cells (Figure 1B). We found that the apical site of  
87 the epithelium mainly consists of ciliated and nonciliated goblet cells (Figures 1C and D).  
88 Studies have shown that mucin 5AC (MUC5AC) is predominately expressed by airway goblet  
89 cells and that mucin 5B (MUC5B) is expressed by goblet cells of submucosal glands (Whitsett,  
90 2018). Club cells are the progenitors of goblet cells, which might express both MUC5AC and  
91 MUC5B (Kiyokawa and Morimoto, 2020; Okuda et al., 2019). As expected, we found

92 heterogeneity in the cell population with differential expression of common goblet cell markers  
93 (Figure 1E) (Lukassen et al., 2020). Basal cells are known for their self-renewal property and  
94 give rise to multiple types of differentiated airway epithelial cells (Crystal, 2014). For the  
95 detection of basal cells, we sectioned the epithelium and stained the sections for the basal cell  
96 marker P63 (Persson et al., 2014; Wang et al., 2002). We found that basal cells reside at the basal  
97 membrane of both epithelia and that the COPD epithelium has more basal cells than the healthy  
98 epithelium as it is known from respiratory epithelium of COPD patients (Figure 1F) (Higham et  
99 al., 2019; Polosukhin et al., 2011).

100 COPD is associated with abnormal airway and alveolar responses during exposure to  
101 noxious stimuli (Brusselle et al., 2011). Because our COPD airway epithelium model was  
102 differentiated from NHBE cells, it should recapitulate the bronchial airway phenotypes instead of  
103 the alveolar phenotype as more commonly associated with emphysema (Barnes, 2013). To  
104 determine whether our in vitro COPD airway epithelium model recapitulates some of the  
105 bronchial pathophysiological characteristics of COPD, we focused on two different aspects:  
106 goblet cell hyperplasia and squamous metaplasia. First, we compared the number of MUC5AC<sup>+</sup>  
107 or MUC5B<sup>+</sup> goblet cells between healthy and COPD epithelia. We found a higher ratio of goblet  
108 cells in the COPD airway epithelium (Figures 1G and H). The higher number of goblet cells in  
109 the COPD epithelium suggests a persistent goblet cell differentiation, which results in goblet cell  
110 hyperplasia (Kim et al., 2015; Reid et al., 2018; Shaykhiev, 2019). Indeed, we found a patch of  
111 higher number of goblet cells with extensive mucus secretion in the COPD epithelium (Figure  
112 1I, center). We also found an apparent loss of pseudostratified epithelium accompanied by  
113 squamous metaplasia in the COPD epithelium, which is a common pathological phenotype in  
114 COPD (Figure 1I, right) (Rigden et al., 2016).

115 To determine the biophysical properties of these respiratory epithelia, we assessed the  
116 tissue membrane integrity (transepithelial electrical resistance, TEER) and ciliary function  
117 (ciliary beat frequency, CBF) and found no significant difference in these biophysical properties  
118 between healthy and COPD epithelia (Figures 1J and K). These results indicated that NHBE  
119 cells from patients with COPD produced a mix of pseudostratified and stratified highly  
120 differentiated mucociliary epithelium with appropriate biophysical properties.

121  
122 **ACE2 and TMPRSS2 are expressed at higher levels in goblet cells.** SARS-CoV-2 infects the  
123 human airway epithelium, and virus entry depends on the host cell receptors ACE2 and its co-  
124 factor TMPRSS2 (Hoffmann et al., 2020). We quantified the ACE2 transcript levels in a lung  
125 epithelial cell line (A549 cells) and primary NHBE cells in a monolayer or in the differentiated  
126 airway epithelium by real-time PCR. We did not detect ACE2 transcripts in the A549 cells  
127 (Figure S1A), which might indicate low or no expression of ACE2 confirming previous data  
128 (Blanco-Melo et al., 2020; Harcourt et al., 2020; Hoffmann et al., 2020; Jia et al., 2005).  
129 However, we detected ACE2 transcripts in primary NHBE cells in both the monolayer and  
130 differentiated airway epithelium (Figure S1A). Despite their similar biophysical properties  
131 (tissue barrier integrity and ciliary function, Figures 1J and K, respectively), ACE2 expression  
132 was higher in the COPD epithelium compared to those derived from a healthy donor (Figures  
133 S1A-C). We then visualized the expression of ACE2 in the airway epithelium by  
134 immunofluorescence imaging. We observed ACE2 expression in both the healthy and COPD  
135 airway epithelia and found that ACE2 expression hardly overlapped with cilia on the apical site  
136 of the epithelium (Figures 2A and S1D). Nevertheless, low levels of ACE2 expression were

137 observed on ciliated cells in our model (Figure S1E). These results suggest that the SARS-CoV-2  
138 entry receptor ACE2 is mainly expressed on non-ciliated cells in the respiratory epithelium.

139 Because ACE2 staining hardly overlapped with acetyl-alpha-tubulin, we tested the  
140 expression of ACE2 along with that of the goblet and club cell markers MUC5AC and MUC5B  
141 (Lukassen et al., 2020). Indeed, ACE2 overlapped with MUC5AC (Figure 2B) and MUC5B  
142 (Figures 2C and S1F). We also compared ACE2 expression with the expression of E-cadherin  
143 and Zonula occludens-1 (ZO-1), markers for adherens junction and tight junction proteins,  
144 respectively. The results showed that ACE2 expression did not overlap with apical tight  
145 junctions or adherent junctions (Figure S2), which suggests that ACE2 expression is primarily  
146 located within the cellular boundary and does not impact the tissue barrier integrity of the  
147 respiratory epithelium. Overall, ACE2 expression was higher in the COPD than in the healthy  
148 epithelium (Figures 2 and S1-2), which is likely due to the presence of goblet cell hyperplasia in  
149 the COPD epithelium and thus a higher number of goblet cells.

150

151 TMPRSS2 is an important host co-factor for SARS-CoV-2 entry into target cells  
152 (Hoffmann et al., 2020; Lukassen et al., 2020; Shulla et al., 2011). We visualized TMPRSS2 in  
153 the apical site of the airway epithelium by staining with anti-TMPRSS2 and found that  
154 TMPRSS2 expression hardly overlapped with cilium (Figure 3A). We then tested the expression  
155 of TMPRSS2 along with that of the goblet cell markers MUC5AC and MUC5B. Indeed,  
156 TMPRSS2 overlapped with MUC5AC (Figure 3B) and MUC5B (Figures 3C). Therefore, it  
157 appears that both TMPRSS2 and ACE2 are expressed on the same cell surface (Figures 2 and 3).  
158 These results indicate that goblet cells may be a novel target of SARS-CoV-2 infection in the  
159 respiratory epithelium.

160

161 **SARS-CoV-2 infects goblet cells.** Although we confirmed that SARS-CoV-2 entry receptors are  
162 expressed at higher levels on nonciliated goblet cells, a number of previous studies have  
163 suggested that SARS-CoV-2 targets ciliated cells (Hou et al., 2020; Lamers et al., 2020).  
164 Therefore, we first examined whether SARS-CoV-2 infects nonciliated goblet cells. We infected  
165 the apical side of the airway epithelium with SARS-CoV-2 at a multiplicity of infection of 0.1  
166 (MOI = 0.1). At 4 days post infection (DPI), we fixed the cells and stained them for SARS-CoV-  
167 2 nucleoprotein (N) and a ciliated cell marker. The results revealed that SARS-CoV-2 infects  
168 both healthy and COPD epithelium and causes a substantial cytopathic effect (CPE) (Figures  
169 S3A and B). SARS-CoV-2 infection was higher in the COPD epithelium than in the healthy  
170 epithelium, as will be addressed later in the manuscript. Although in some cases the virus-  
171 induced extensive CPE made it difficult to distinguish SARS-CoV-2 cell tropism, we focused on  
172 multiple random areas with less CPE but virus infection. We found that SARS-CoV-2 infects  
173 nonciliated cells in both healthy and COPD epithelium (Figure 4A). We also used a second  
174 detection method to visualize viral and cellular markers in cross sections of the epithelium.  
175 Immunohistochemistry-based staining confirmed the extensive CPE induced by SARS-CoV-2 in  
176 both healthy and COPD epithelium. Apparently, SARS-CoV-2 infected both ciliated and  
177 nonciliated epithelial cells in the airway epithelium (Figure 4B). Using staining strategies similar  
178 to those described before, we found that SARS-CoV-2 infects MUC5B-positive (Figures 4C and  
179 D) and MUC5AC-positive (Figure 4E) goblet cells. To determine whether SARS-CoV-2 infects  
180 basal cells, we stained the sectioned epithelium for P63 and the SARS-CoV-2 spike (S) protein.  
181 We did not observe any overlap between the SARS-CoV-2 S protein and the basal cell marker

182 (Figure S4). These results suggest that SARS-CoV-2 infects nonciliated goblet cells in addition  
183 to ciliated cells.

184

185 **SARS-CoV-2 induces syncytia and cell sloughing in the airway epithelium.** To determine  
186 whether SARS-CoV-2 infection in the airway epithelium recapitulates the virus-induced  
187 pathophysiology in the lung, we examined the infected epithelium under a confocal microscope  
188 and found that SARS-CoV-2 infection causes substantial damage to the apical site of the infected  
189 epithelium, as confirmed by extensive CPE in both healthy and COPD epithelium (Figure S3).  
190 We also found substantial mucus secretion due to SARS-CoV-2 infection. The apical damage of  
191 the SARS-CoV-2-infected epithelium included loss of cellular junctions, loss of ciliary damage,  
192 substantial mucus production, and the protraction of nuclei, which are all common features  
193 observed in SARS-CoV-2-infected lungs (Schaefer et al., 2020). Additionally, we investigated  
194 whether SARS-CoV-2-infected cells in the epithelium might form syncytium (multinucleated  
195 cell), a hallmark of SARS-CoV-2 infection in the lung (Giacca et al., 2020) that had also been  
196 reported for SARS-CoV-1 (Franks et al., 2003). Indeed, we found that SARS-CoV-2-infected  
197 cells formed syncytia in both healthy and COPD epithelia (Figure 5A and B). Cell sloughing has  
198 been reported from lung autopsy findings of SARS-CoV-2-infected patients (Schaefer et al.,  
199 2020). Therefore, we examined whether SARS-CoV-2 infection in our epithelium model  
200 recapitulates cell sloughing. Indeed, we found that SARS-CoV-2 induces cell sloughing in both  
201 healthy and COPD epithelia as confirmed by two independent methods, immunofluorescence  
202 and IHC (Figures 5C and D). These results demonstrate that hallmark pathological features of  
203 SARS-CoV-2 are recapitulated in the infected airway epithelium model.

204

205 **SARS-CoV-2 replicates higher and exacerbates pathophysiology in COPD epithelium.** To  
206 determine whether SARS-CoV-2 replicates better in the COPD epithelium, we titered SARS-  
207 CoV-2 in the apical wash of the infected epithelium and found that SARS-CoV-2 replication was  
208 increased by almost a log in the COPD compared to the healthy epithelium (Figure 6A). In  
209 addition, we found a squamous metaplasia in SARS-CoV-2-infected COPD epithelium which  
210 was rather infrequently found in the SARS-CoV-2-infected healthy epithelium (Figures 1I; 4B,  
211 D, and E, and 5B and D) (Borczuk et al., 2020). Squamous metaplasia is known to increase  
212 bronchial wall thickening as seen in bronchitis (Randell, 2006; Reid et al., 2018; Rigden et al.,  
213 2016). As tracheobronchitis is one of the most common histopathological features in the  
214 COVID-19 disease fatalities (Martines et al., 2020), we evaluated whether SARS-CoV-2  
215 infection increases height of the epithelium. First, there was a substantial increase in squamous  
216 metaplasia in the COPD epithelium due to SARS-CoV-2 infection (Figure S5). Second, the  
217 increased metaplasia apparently changed the morphology of the nonciliated goblet cells in the  
218 infected COPD epithelium (Figures 6B and C). Whether this change in the goblet cell  
219 morphology impacted the mucus hyperplasia remains to be determined. Third, in contrast to the  
220 healthy epithelium, SARS-CoV-2 induced higher squamous metaplasia in the infected COPD  
221 epithelium and caused a substantial increase in the height of the epithelium (Figure 6D). These  
222 results suggest that SARS-CoV-2 replicates better in the COPD epithelium and exacerbates  
223 pathophysiology in the infected airway epithelium.

224

## 225 **Discussion.**

226 Here, we have shown that the COPD epithelium model recapitulates the bronchial  
227 biophysical and pathophysiological characteristics of COPD, such as goblet cell hyperplasia and

228 squamous metaplasia (Gohy et al., 2019; Kim et al., 2015; Reid et al., 2018; Rigden et al., 2016).  
229 A previous report suggested the presence of altered ciliated cells in COPD airway epithelium  
230 (Gohy et al., 2019), which was not observed in our model. The duration of cell differentiation  
231 may be the reason, as we differentiated NHBE cells for four weeks that may require to see  
232 terminal differentiation (including ciliogenesis) (Gohy et al., 2019). We used an air-liquid  
233 interface (ALI) culture method to generate multi-cellular diversity and physiologic functioning  
234 airway epithelium that resembles the airway surface in vivo (Fulcher et al., 2005; Pawlina, 2016;  
235 Rayner et al., 2019). One of the limitations in the ALI culture research is passaging of primary  
236 NHBE cells may impact on their ability to differentiate into airway epithelium. We could  
237 demonstrate that primary NHBE cells obtained after four passages without using any additional  
238 supplements can still be differentiated into human airway epithelium (Rayner et al., 2019). In a  
239 separate study, we confirmed that passaging NHBE cells up to four times has insignificant effect  
240 on the whole-genome transcriptome by comparing transcriptome profiles of each passage cells  
241 (data not shown). The ability to expand primary cells that also form fully differentiated  
242 mucociliary epithelium reduces repeat sample collections from patients where samples are  
243 difficult and limited, such as infants and deceased patients (Rayner et al., 2019; Wolf et al.,  
244 2017). Our results demonstrate primary NHBE cells either from healthy or a COPD patient can  
245 be passaged up to four times and that normal epithelial phenotypic features are maintained in  
246 passaged primary NHBE cells.

247         One emergent question is why the human-to-human transmission of SARS-CoV-2 is  
248 much higher compared to SARS-CoV-1, although both viruses share ACE2 as cell surface  
249 receptor and use TMPRSS2 to facilitate their entry into the host cell (Hoffmann et al., 2020;  
250 Lukassen et al., 2020). The SARS-CoV-2 spike protein has an additional furin cleavage site that

251 is absent in SARS-CoV-1, and it is hypothesized that furin cleavage facilitates human-to-human  
252 transmission (Coutard et al., 2020; Lukassen et al., 2020). We found that SARS-CoV-2 infected  
253 both ciliated cells and nonciliated goblet cells, but not basal cells in the airway epithelium.  
254 Although SARS-CoV-2 may preferentially infect goblet cells due to the higher expression of  
255 ACE2 and TMPRSS2, further studies are needed to confirm temporal and spatial regulations of  
256 SARS-CoV-2 infection in the airway epithelium. The major function of goblet cells in the lung  
257 epithelium is mucin production to trap pathogens, dust, and particles, which are cleared by a  
258 process known as mucociliary clearance (Rogers, 2003). The possibility that SARS-CoV-2  
259 infects goblet cells could explain the presence of viral RNA in sputum (Wang et al., 2020) and  
260 might explain the easy transmission of the virus from person to person. While we are preparing  
261 our manuscript, Hao et al., have shown that goblet cells are permissive to SARS-CoV-2 infection  
262 (Hao et al., 2020). As SARS-CoV-1 infection is limited to ciliated cells (Sims et al., 2005), we  
263 think that SARS-CoV-2 infection in goblet cells could explain why SARS-CoV-2 is more  
264 transmissible than SARS-CoV-1. Influenza A virus infects goblet cells in addition to ciliated  
265 cells (Matrosovich et al., 2004), whereas respiratory syncytial virus (RSV) infects only ciliated  
266 cells (Zhang et al., 2002). Therefore, virus-specific preferential cell tropism in the lung could  
267 explain the difference in respiratory virus pathogenicity and transmissibility.

268 Our airway epithelium model recapitulated some SARS-CoV-2-induced lung  
269 histopathological findings, such as prominent nucleoli (Schaefer et al., 2020), cytoplasmic  
270 vacuolation, multinucleated giant cells (Falasca et al., 2020), squamous metaplasia (Martines et  
271 al., 2020) and epithelial cell sloughing, which is the most common finding (Bradley et al., 2020).  
272 SARS-CoV-2 infection in the bronchial epithelium models induced a substantial amount of cell  
273 syncytium formation and cell sloughing, which indicates that tracheobronchial cells are highly

274 associated with virus-induced pathogenesis. Therefore, our data suggest that bronchial cells are  
275 equally important to alveolar cells in the SARS-CoV-2 pathogenesis (Martines et al., 2020). In  
276 patients with COPD, goblet cell hyperplasia is a common clinical manifestation, and an  
277 increasing number of goblet cells results in more mucus production (Shaykhiev, 2019). Because  
278 we have shown that SARS-CoV-2 replicated at a higher rate in the COPD epithelium, we believe  
279 that goblet cell hyperplasia is responsible for this phenomenon and may explain why COPD  
280 patients are at higher risk for severe outcome of COVID-19. Interestingly, we found that SARS-  
281 CoV-2 infection induced “squamous metaplasia” in the COPD epithelium. Squamous metaplasia  
282 in the columnar epithelium correlates with increased severity of airway obstruction in COPD  
283 (Araya et al., 2007). Although squamous metaplasia is one of the histopathological findings in  
284 the SARS-CoV-2 infected patient fatalities (Martines et al., 2020), our results provide evidence  
285 for the first time that SARS-CoV-2 infection increases squamous metaplasia, which may result in  
286 bronchitis in the infected COPD patients. In fact, tracheobronchitis is one of the most common  
287 histopathological features in the COVID-19 disease fatalities (Martines et al., 2020). No SARS-  
288 CoV-2 infectious virion was detected in the basal medium of the infected healthy and COPD  
289 epithelia, which might suggest that the initial virus-induced substantial damage was limited at the  
290 apical site.

291 Immune responses to viral infection play a critical role in determining the clinical  
292 outcomes of SARS-CoV-2 infection (Huang et al., 2020). Unfortunately, our airway epithelium  
293 model lacks both resident and infiltrating immune cells (dendritic cells, macrophages, and  
294 lymphocytes, etc.) and is devoid of the endothelial layer, and therefore cannot study the impact  
295 of immune responses on the SARS-CoV-2 infections. However, we can provide inferences based  
296 on the detection of immunoregulatory factors (chemokines and cytokines), but these hypotheses

297 remain to be confirmed. Overall, we believe that the airway epithelium model provides an  
298 excellent tool for demystifying some of the SARS-CoV-2 pathophysiological features and  
299 identifying and testing novel therapeutics against the virus.

300 In conclusion, we developed in vitro lung airway epithelium models from passaged  
301 primary NHBE cells of either a healthy or a COPD patient. Our studies revealed SARS-CoV-2  
302 infection of goblet cells leading to virus-induced syncytium formation and cell sloughing in the  
303 airway epithelium. We found that SARS-CoV-2 replicates better COPD airway epithelium likely  
304 due to COPD associated goblet cell hyperplasia. Thus, we postulate that goblet cells play a  
305 critical role in SARS-CoV-2 infection of the lung and are responsible for more severe outcome  
306 of SARS-CoV-2 infection in COPD patients.

307

#### 308 **Figure legends.**

309 **Figure 1. The airway epithelium model recapitulates the bronchial characteristics of**  
310 **COPD. (A).** Airway epithelium derived from differentiated NHBE cells obtained from a healthy  
311 adult or COPD patient were fixed, embedded in paraffin, sectioned and stained with hematoxylin  
312 and eosin (H&E). The nuclei are stained dark-purple, and the cytoplasmic components are pink.  
313 Bar = 50  $\mu$ m. **(B).** The sectioned epithelia were stained with Alcian blue. Mucosubstances are  
314 stained blue, whereas the cytoplasmic components are pale pink, and the nuclei are pink/red. Bar  
315 = 50  $\mu$ m. **(C).** The apical sites of the airway epithelia were fixed, permeabilized and stained for  
316 the goblet cell marker MUC5AC (anti-MUC5AC, green), the ciliated cell marker acetyl-alpha  
317 tubulin (anti-acetyl-alpha tubulin, cyan), and F-actin (rhodamine phalloidin, red); the nuclei were  
318 also stained with DAPI (blue). Bar = 10  $\mu$ m. **(D).** The sectioned epithelia were stained for the  
319 ciliated cell marker acetyl-alpha tubulin (anti-acetyl-alpha tubulin, cyan), the goblet cell marker

320 MUC5AC (anti-MUC5AC, green), and F-actin (rhodamine phalloidin, red); the nuclei were also  
321 stained with DAPI (blue). Bar = 20  $\mu$ m. **(E)**. The apical sites of the airway epithelia were fixed  
322 and stained for two goblet cell markers, MUC5AC and MUC5B [anti-MUC5AC (green) and  
323 anti-MUC5B (cyan), respectively] and F-actin (rhodamine phalloidin, red); the nuclei were also  
324 stained with DAPI (blue). Bar = 10  $\mu$ m. **(F)**. The sectioned epithelia were stained for the basal  
325 cell marker P63 (anti-P63, green), the goblet cell marker MUC5B (anti-MUC5B, cyan), and F-  
326 actin (rhodamine phalloidin, red); the nuclei were also stained with DAPI (blue). Bar = 20  $\mu$ m.  
327 **(G)**. The MUC5B<sup>+</sup> goblet cells were counted from tiled images of the airway epithelium stained  
328 for MUC5B (anti-MUC5B, cyan) (described above) obtained with a Leica DMI8 epifluorescence  
329 microscope. A total of approximately 3,500 cells were counted from each epithelium to  
330 determine the ratio. **(H)**. The MUC5AC<sup>+</sup> goblet cells were counted from random fields in  
331 confocal images of the airway epithelium stained for MUC5AC (anti-MUCAC, cyan) (described  
332 above). A total of approximately 1,500 cells were counted from each epithelium to determine the  
333 ratio. **(I)**. The sectioned epithelia were stained for MUC5B (anti-MUC5B, cyan); the nuclei were  
334 stained with DAPI (blue). Bar = 20  $\mu$ m. **(J)**. Transepithelial electrical measurements (TEERs) of  
335 the airway epithelia were obtained. The data were obtained by combining three independent  
336 Transwell reads, and each Transwell read was an average of three independent reads. The error  
337 bars represent the SEMs. **(K)**. The ciliary beat frequency (CBF) was measured on the airway  
338 epithelia. The data were obtained by combining three independent Transwell reads, and each  
339 Transwell read was an average of six random point reads. The error bars represent the SEMs.  
340 The statistical significance was determined by unpaired two-tailed t-tests. The results from one  
341 independent experiment are shown.

342

343 **Figure 2. ACE2 is expressed at higher levels in goblet cells.** The airway epithelia were  
344 generated and fixed as described in Figure 1 (A) Cells were stained for ACE2 (anti-ACE2,  
345 green), cilia (anti-acetyl-alpha tubulin, cyan) F-actin (rhodamine phalloidin, red) and nuclei  
346 (DAPI, blue). (B). Cells were stained for ACE2 (anti-ACE2, green), MUC5AC<sup>+</sup> goblet cells  
347 (anti-MUC5AC, cyan) F-actin (rhodamine phalloidin, red) and nuclei (DAPI, blue). (C). Cells  
348 were stained for ACE2 (anti-ACE2, green), MUC5B<sup>+</sup> goblet cells (anti-MUC5B, cyan), F-actin  
349 (rhodamine phalloidin, red) and nuclei (DAPI, blue). Bar =10 μm. See also Figures S1 and S2.

350

351 **Figure 3. TMPRSS2 is expressed at higher levels in goblet cells.** (A). The airway epithelia  
352 (described in Figure 1) were stained for cilia (anti-acetyl-alpha tubulin, cyan), TMPRSS2 (anti-  
353 TMPRSS2, green), and F-actin (rhodamine phalloidin, red); the nuclei were stained with DAPI  
354 (blue). (B). The airway epithelia were stained for the identification of MUC5AC<sup>+</sup> goblet cells  
355 (anti-MUC5AC, cyan), TMPRSS2 (anti-TMPRSS2, green), F-actin (rhodamine phalloidin, red)  
356 and nuclei (DAPI, blue). (C). The airway epithelia were stained to identify MUC5B<sup>+</sup> goblet cells  
357 (anti-MUC5B, cyan), TMPRSS2 (anti-TMPRSS2, green), F-actin (rhodamine phalloidin, red)  
358 and nuclei (DAPI, blue). Bar =10 μm.

359

360 **Figure 4. SARS-CoV-2 infects goblet cells.** (A). The airway epithelia were mock-infected or  
361 infected with SARS-CoV-2 at an MOI of 0.1. At 4 days post infection (DPI), the epithelia were  
362 fixed, permeabilized, and stained for the identification of cilia (anti-acetyl-alpha tubulin, cyan),  
363 SARS-CoV-2 N (anti-N, green), F-actin (rhodamine phalloidin, red) and nuclei (DAPI, blue).  
364 The arrows indicate SARS-CoV-2-infected nonciliated cells. (B). At 4 DPI, the epithelia  
365 (described in A) were stained for the goblet cell marker MUC5B (anti-MUC5B, cyan), SARS-

366 CoV-2 N (anti-N, green), and F-actin (rhodamine phalloidin, red); the nuclei were stained with  
367 DAPI (blue). The arrows indicate SARS-CoV-2-infected MUC5B<sup>+</sup> goblet cells. **(C)**. At 4 DPI,  
368 the epithelia (described in A) were embedded in paraffin, sectioned and stained for the detection  
369 of cilia (anti-acetyl-alpha tubulin, cyan) and SARS-CoV-2 N (anti-N, green); the nuclei were  
370 stained with DAPI (blue). The arrows indicate SARS-CoV-2-infected nonciliated cells. **(D)**. At 4  
371 DPI, the sectioned epithelia were stained for the goblet cell marker MUC5AC (anti-MUC5AC,  
372 cyan) and SARS-CoV-2 N (anti-N, green); the nuclei were also stained with DAPI (blue). The  
373 arrows indicate SARS-CoV-2-infected MUC5AC<sup>+</sup> goblet cells. **(E)**. At 4 DPI, the sectioned  
374 epithelia were stained for the goblet cell marker MUC5B (anti-MUC5B, cyan) and SARS-CoV-2  
375 N (anti-N, green); the nuclei were also stained with DAPI (blue). The arrows indicate SARS-  
376 CoV-2-infected MUC5B<sup>+</sup> goblet cells. (A and B) Bar = 5 μm. (C, D and E) Bar = 20 μm. See  
377 also Figures S3 and S4.

378

379 **Figure 5. SARS-CoV-2 induces syncytia and cell sloughing.** **(A)**. The airway epithelia (mock  
380 or infected; described in Figure 4) were stained for SARS-CoV-2 N (anti-N, green) and F-actin  
381 (rhodamine phalloidin, red); the nuclei were also stained with DAPI (blue). The arrows indicate  
382 syncytia. Bar = 5 μm. **(B)**. At 4 DPI, the sectioned epithelia were stained for the goblet cell  
383 marker MUC5AC (anti-MUC5AC, cyan) and SARS-CoV-2 N (anti-N, green), and the nuclei  
384 were also stained with DAPI (blue). The arrows indicate syncytia. Bar = 20 μm. **(C)**. At 4 DPI,  
385 the airway epithelia were stained for SARS-CoV-2 N (anti-N, green) and F-actin (rhodamine  
386 phalloidin, red), and the nuclei were stained with DAPI (blue). The arrows indicate cell  
387 sloughing. Bar = 5 μm. **(D)**. At 4 DPI, the sectioned epithelia were stained for cilia (anti-acetyl-

388 alpha tubulin, cyan) and SARS-CoV-2 N (anti-N, green), and the nuclei were stained with DAPI  
389 (blue). The arrows indicate cell sloughing. Bar = 20  $\mu$ m.

390

391 **Figure 6. SARS-CoV-2 replicates at a higher rate and increases squamous metaplasia in the**  
392 **COPD epithelium. (A).** The apical wash of the SARS-CoV-2-infected airway epithelia  
393 (described in Figure 4) was collected, and SARS-CoV-2 titration was performed based on the  
394 tissue culture infective dose 50 (TCID<sub>50</sub>). The results from an independent experiment (n=3) are  
395 shown. The error bars show the SEMs. **(B).** The sectioned epithelia (described in Figure 4) were  
396 stained with Alcian blue. Bar = 50  $\mu$ m. **(C).** At 4 DPI, the sectioned epithelia (COPD epithelia  
397 after mock or SARS-CoV-2 infection) were stained for the goblet cell marker MUC5B (anti-  
398 MUC5B, cyan) and SARS-CoV-2 N (anti-N, green), and the nuclei were stained with DAPI  
399 (blue). Bar = 20  $\mu$ m. **(D).** The height of the airway epithelia (described in C) was measured from  
400 the images (n=5), the average of 12 points was plotted. See also Figure S5.

401

402 **Figure S1. ACE2 expression is higher in the COPD airway epithelium. (A)** ACE2 mRNA  
403 expression in total RNA extracted from the lung epithelial cell line (A549 cells) and primary  
404 NHBE cells from healthy adults and patients with COPD in monolayers or differentiated into  
405 airway epithelia was quantified by real-time PCR. The data were plotted as expression levels  
406 normalized to those in the NHBE healthy monolayer. The data were obtained by combining the  
407 quadruplet technical replicates of each sample. The graph represents the results from two  
408 independent real-time PCR runs. **(B).** ACE2 was detected in the airway epithelium (obtained  
409 after 4 weeks of differentiation of NHBE cells) by Western blotting. **(C).** The ACE2 signal  
410 (shown in B) was quantified (normalized to the alpha-tubulin level) and plotted relative to that in

411 the healthy epithelium. **(D)**. The apical sites of the airway epithelia were fixed and stained for  
412 ACE2 (anti-ACE2, green), cilia (anti-acetyl-alpha tubulin, cyan) and F-actin (rhodamine  
413 phalloidin, red). Deconvoluted Z-stack images are presented in the 3D view. **(E)**. The apical sites  
414 of the airway epithelia were fixed and stained for cilia (anti-acetyl-alpha tubulin, cyan), ACE2  
415 (anti-ACE2, green), F-actin (rhodamine phalloidin, red) and nucleus (DAPI, blue). Bar = 15  $\mu$ m.  
416 **(F)**. The airway epithelia (described in D) were stained for ACE2 (anti-ACE2, green), MUC5B  
417 (anti-MUC5B, cyan) and F-actin (rhodamine phalloidin, red). Deconvoluted Z-stack images are  
418 presented in the 3D view.

419

420 **Figure S2. ACE2 expression within the goblet cell boundary.** The airway epithelia (obtained  
421 after 4 weeks of differentiation of NHBE cells) were fixed and stained for ACE (anti-ACE2  
422 antibody, green) and MUC5B (anti-MUC5B, cyan) or ZO-1 (anti-ZO-1 antibody, cyan) or e-  
423 cadherin (anti-e-cadherin antibody, cyan). F-actin (red) and nuclei (blue) were stained with  
424 rhodamine phalloidin and DAPI, respectively. The images represent multiple random areas  
425 obtained from an independent experiment. Bar = 10  $\mu$ m.

426

427 **Figure S3. SARS-CoV-2 induces a cytopathic effect in the airway epithelia.** The airway  
428 epithelia were mock-infected or infected with SARS-CoV-2 at an MOI of 0.1. At 4 days post  
429 infection (DPI), the epithelia were fixed, embedded in paraffin, sectioned, and stained for the  
430 basal cell marker P63 (anti-P63, green), SARS-CoV-2 spike (S) (anti-S, cyan), and F-actin  
431 (rhodamine phalloidin, red); the nuclei were stained with DAPI (blue). Bar = 20  $\mu$ m.

432

433 **Figure S4. SARS-CoV-2 does not infect basal cells in the airway epithelia.** The airway  
434 epithelia were mock-infected or infected with SARS-CoV-2 at an MOI of 0.1. At 4 days post  
435 infection (DPI), the epithelia were fixed, permeabilized, and stained for cilia (anti-acetyl-alpha  
436 tubulin, cyan), SARS-CoV-2 N (anti-N, green), and F-actin (rhodamine phalloidin, red); the  
437 nuclei were stained with DAPI (blue). The images represent multiple independent random areas  
438 from an independent experiment. Bar = 30  $\mu$ m.

439

440 **Figure S5. SARS-CoV-2 increases squamous metaplasia in the COPD airway epithelia.** The  
441 airway epithelia were mock-infected or infected with SARS-CoV-2 at an MOI of 0.1. At 4 days  
442 post infection (DPI), the epithelia were fixed, permeabilized, and stained with hematoxylin and  
443 eosin (H&E). Bar = 50  $\mu$ m.

444

#### 445 **Graphical Abstract.**

#### 446 **Highlights:**

- 447 1. The airway epithelium model recapitulates many bronchial pathological characteristics of  
448 COPD, such as goblet cell hyperplasia and squamous metaplasia
- 449 2. ACE2 and TMPRSS2 are highly expressed on nonciliated goblet cells
- 450 3. SARS-CoV-2 infects goblet cells and induces syncytium formation and cell sloughing
- 451 4. SARS-CoV-2 replicates at a higher rate in the COPD epithelium and increases squamous  
452 metaplasia

#### 453 **In Brief:**

454 Osan et al. showed that SARS-CoV-2 preferentially infects and replicates in nonciliated goblet  
455 cells inducing syncytium formation and cell sloughing. Our results suggest that goblet cells play  
456 a critical role in SARS-CoV-2-induced pathophysiology in the lung.

457

458 **Acknowledgments.** We thank the Microscopy Core (UND, Grand Forks) funded by NIH  
459 P20GM103442 of the INBRE program for providing access to an Olympus FV300 confocal  
460 microscope and Dr. Swojani Shrestha for the technical support provided. Histological services  
461 were provided by Histology Core (UND, Grand Forks) funded by NIH P20GM113123, NIH  
462 DaCCoTA CTR, NIH U54GM128729, and UNDSMHS funds. We also thank the Imaging Core  
463 (UND, Grand Forks) funded by NIH P20GM113123, NIH U54GM128729, and UNDSMHS  
464 funds for the IMARIS image analyses. We thank John Lee, Information Resources, UND, for  
465 preparing the graphical abstract. This work was funded by NIH/NIGMS P20GM113123 and in  
466 part by the Intramural Research Program of NIAID, NIH.

467

468 **Author contributions.** M.M., J.K.O., and S.N.T. conceived the project and designed the  
469 experiments. K.L.B. provided the primary cells as well as training and guidance on primary cell  
470 differentiation. M.M., J.K.O., and S.N.T. performed the experiments. S.N.T. generated the  
471 confocal images. F.F. and H.F. performed the virus infection experiments in the BSL-4  
472 laboratory. J.K.O., B.A.D., and K.J. generated the IHC images, B.A.D. performed the H&E and  
473 Alcian Blue staining, and M.M., J.K.O., and S.N.T. wrote the paper. M.M. and H.F. reviewed  
474 and edited the paper.

475 **STAR METHOD**

476 **KEY RESOURCE TABLE**

REAGENT or RESOURCE	SOURCE	IDENTIFIER
<b>Antibodies</b>		
Rabbit monoclonal Anti-E-cadherin	Cell Signaling Technology	Cat#3195S; Clone 24E10; RRID:AB_2291471
Rabbit monoclonal Anti-MUC5B	Atlas Antibodies	Cat# HPA008246; RRID:AB_1854203
Mouse polyclonal Anti-MUC5AC	Abnova	Cat# H00004586-A01; RRID:AB_606620
Rabbit monoclonal Anti-MUC5AC	Cell Signaling Technology	Cat#61193; Clone E3O9I; RRID: AB_2799603
Mouse monoclonal Anti- $\alpha$ -tubulin	Sigma-Aldrich	Cat#T6199; RRID:AB_477583
Rabbit polyclonal Anti-ZO-1	Thermo Fisher Scientific	Cat#40-2200; RRID:AB_2533456
Rabbit monoclonal Anti-Acetyl- $\alpha$ - Tubulin	Cell Signaling Technology	Cat#5335; RRID:AB_10544694
Mouse monoclonal Anti-TMPRSS2	Santa Cruz Biotechnology	Cat#sc-515727
Goat polyclonal Anti-ACE2	R and D Systems	Cat# AF933; RRID:AB_355722
Mouse monoclonal Anti-p63	Abcam	Cat# ab735; Clone BC4A4; RRID: AB_305870
Mouse monoclonal Anti-ACE2	R and D Systems	Cat# MAB933; Clone 171606 RRID:AB_2223153
Mouse monoclonal Anti-SARS/SARS- CoV-2 Nucleocapsid protein	Thermo Fisher Scientific	Cat# MA1-7404; Clone B46F RRID:AB_1018422
Rabbit polyclonal Anti-SARS/SARS- CoV-2 Coronavirus Spike Protein	Thermo Fisher Scientific	Cat# PA5-81795; RRID:AB_2788969

Donkey Anti-Goat IgG antibody IRDye 800CW	LI-COR Biosciences	Cat# 926-32214, RRID:AB_621846
Goat Anti-Mouse IgG antibody IRDye 680RD	LI-COR Biosciences	Cat#926-68070;RRID:AB_10956588
Goat anti-Mouse IgG Antibody, Alexa Fluor 488	Thermo Fisher Scientific	Cat# A-11029; RRID:AB_2534088
Goat anti-Rabbit IgG Antibody, Alexa Fluor 647	Thermo Fisher Scientific	Cat# A-21245; RRID:AB_2535813
<b>Critical Commercial Assays</b>		
BCA protein assay kit	Thermo Fisher Scientific	23225
AllPrep DNA/RNA Mini Kit	Qiagen	80204
RNeasy Mini Kit	Qiagen	74104
<b>Virus strains</b>		
SARS CoV-2 WA 1 isolate	Natalie J Thornburg, CDC	GenBank: MN985325.1
<b>Software</b>		
IMARIS 9.5.1	Oxford Instruments	<a href="https://imaris.oxinst.com/">https://imaris.oxinst.com/</a>
Fiji	ImageJ	<a href="https://imagej.net/Downloads">https://imagej.net/Downloads</a>
Prism 8	GraphPad	<a href="https://www.graphpad.com/scientific-software/prism/">https://www.graphpad.com/scientific-software/prism/</a>
Sisson-Ammons Video Analysis (SAVA)	Ammons Engineering	N/A
LASX	Leica Microsystem	N/A
Image Studio 5.2	LI-COR Biosciences	<a href="https://www.licor.com/bio/image-studio/">https://www.licor.com/bio/image-studio/</a>
Photoshop 2020	Adobe	N/A
<b>Experimental models:</b>		

<b>Primary cells/ Cell lines</b>		
Normal Bronchial Epithelial Cells (NHBE C16)	Provided by Dr. Kristina Bailey laboratory	
COPD Bronchial Epithelial Cells	Provided by Dr. Kristina Bailey laboratory	
A549 cells	Provided by Dr. Peter Collins laboratory	
Vero cells	Heinz Feldmann, RML	
<b>Chemical reagents, siRNA and Media</b>		
Airway Epithelial Cell Growth Medium	PromoCell	C21060
PneumaCult™-ALI Medium	Stemcell Technologies	05002
F-12 Medium	Thermo Fisher Scientific	11765054
2-mercaptoethanol	Sigma-Aldrich	M6250
Penicillin-Streptomycin	Thermo Fisher Scientific	15140122
HyClone™ Fetal Bovine Serum	Thermo Fisher Scientific	SH3007103
Amphotericin B	Thermo Fisher Scientific	15290026
Goat Serum Blocking Solution	Vector Laboratories	S-1000-20
PureCol, Bovine Collagen	Cell Systems	5005
NucBlue™ fixed cell stain ReadyProbes	Thermo Fisher Scientific	R37606
ProLong™ Gold anti-fade Mounting	Thermo Fisher Scientific	P36930
Rhodamine Phalloidin (Amanita phalloides)	Cytoskeleton Inc.	PHDR1
16% Formaldehyde (Methanol free)	Polysciences	18814-10
Intercept® (PBS) Blocking Buffer and Diluent Kit	LI-COR Biosciences	927-76003

TrypLE™ Express Enzyme	Thermo Fisher Scientific	12604021
<b>Other</b>		
6.5 mm Transwell® with 0.4 µm Pore Polyester Membrane Insert	Corning	3470
Bolt™ 4-12% Bis-Tris Plus Gels	Thermo Fisher Scientific	NW04120BOX
iBlot™ 2 Transfer Stacks, PVDF	Thermo Fisher Scientific	IB24002
EVOM2 epithelial volt-ohmmeter	World Precision Instruments Inc	177776 AB06J
FV3000 Confocal Laser Scanning Microscope	Olympus Corporation	N/A
Leica DMI8 Inverted Microscope	Leica Microsystem	N/A
Odyssey® CLx Imaging System	LI-COR Biosciences	N/A
Transmission Electron Microscope HT7700	Hitachi	N/A
CFX384 Real-Time PCR System	Bio-Rad	N/A
Epoch microplate spectrophotometer	BioTek	N/A

477

## 478 **RESOURCE AVIALABILITY**

### 479 **Lead Contact**

480 Further information and requests for resources and reagents should be directed to and will be  
481 fulfilled by the lead contact, Masfique Mehedi ([masfique.mehedi@und.edu](mailto:masfique.mehedi@und.edu)).

482

### 483 **Material Availability**

484 The materials and reagents generated in this study will be made available upon installment of a  
485 material transfer agreement (MTA).

486 **Competing interest.** The authors declare no competing interests.

## 487 **EXPERIMENTAL MODEL AND SUBJECT DETAILS**

488 **Cells.** Primary normal human bronchial epithelial (NHBE) cells from either a deidentified  
489 healthy adult (female, aged 52 years, never-smoker) or a patient with chronic obstructive  
490 pulmonary disease (COPD) were obtained under an approved material transfer agreement  
491 (MTA) between the Mehedi Laboratory at University of North Dakota (UND) and Bailey  
492 Laboratory at University of Nebraska Medical Center (UNMC), Omaha, NE. A549 cells (a  
493 human lung epithelial cell line, ATCC-185) were obtained from Dr. Peter Collins at the National  
494 Institutes of Health (NIH), Bethesda, MD, USA. Vero cells used for TCID<sub>50</sub> assay were a  
495 resource of the Feldmann Lab at the Rocky Mountain Laboratories, Hamilton, MT.

496

497 **Virus.** The SARS-CoV-2 isolate nCoV-WA1-2020 (MN985325.1) was kindly provided by CDC  
498 as Vero passage 3 (Harcourt et al., 2020). The virus was propagated once in Vero E6 cells in  
499 DMEM (Sigma) supplemented with 2% fetal bovine serum (Thermo Fisher Scientific), 1 mM L-  
500 glutamine (Thermo Fisher Scientific), 50 U/ml penicillin and 50 µg/ml streptomycin (Thermo  
501 Fisher Scientific) (virus isolation medium). The virus stock used in this study was 100%  
502 identical to the initially deposited GenBank sequence (MN985325.1); sequencing did not detect  
503 any virus stock contaminants.

504

505 **Biosafety Statement.** Work with SARS-CoV-2 was performed in the high biocontainment  
506 facilities at the Rocky Mountain Laboratories (RML), NAID, NIH in Hamilton, MT. All  
507 infectious work followed standard operating procedures (SOPs) approved by the Institutional  
508 Biosafety Committee.

509

510 **METHOD DETAILS:**

511 **Cell culture.** We passaged the primary NHBE cells (passage 1) three times before differentiating  
512 them (passage 4) into a pseudostratified epithelium. For each passage, the cells were grown in a  
513 100-mm culture dish (Corning Inc.) precoated with PurCol (Advanced Biometrics). The cells  
514 were maintained in airway epithelial cell (AEC) growth medium (PromoCell) containing AEC  
515 supplements (PromoCell), 2% penicillin/streptomycin (Thermos Fisher Scientific), and 1%  
516 amphotericin B (Thermos Fisher Scientific) (complete AEC medium) at 37°C in an incubator  
517 with 5% CO<sub>2</sub>. The cells were grown to 90% confluency, and the medium was changed every  
518 other day. Confluent monolayers of cells were dissociated with 5 ml of TrypLE (Thermo Fisher  
519 Scientific) and pelleted, and one-third of the cells were reseeded in a culture dish containing  
520 complete AEC medium for passaging. A549 cells were grown in F-12 medium (Thermo Fisher  
521 Scientific) with 10% HyClone fetal bovine serum (GE Healthcare), 2% penicillin/streptomycin,  
522 and 1% amphotericin B.

523

524 **Air-liquid interface (ALI) culture.** Transwells (6.5 mm) with 0.4- $\mu$ m-pore polyester membrane  
525 inserts (Corning Inc.) were coated with PureCol for 20 minutes before cell seeding. NHBE cells  
526 ( $5 \times 10^4$ ) suspended in 200  $\mu$ l of complete AEC medium were seeded in the apical part of a  
527 Transwell. Subsequently, 500  $\mu$ l of complete AEC medium was added to the basal part of the  
528 Transwell. When the cells formed a confluent layer on the Transwell insert, the AEC medium  
529 was removed from the apical part, and PneumaCult-ALI basal medium (Stemcell Technologies)  
530 with the required supplements (Stemcell Technologies), 2% penicillin/streptomycin and 1%  
531 amphotericin B (complete ALI basal medium) was added to the basal part. The ALI medium in

532 the basal part was changed every other day, and the apical surface was washed with 1x  
533 Dulbecco's phosphate-buffered saline (DPBS) (Thermo Fisher Scientific) once per week initially  
534 but more frequently when more mucus was observed on later days. However, the thickness of the  
535 mucus was not determined. All the cells were differentiated for at least 4 weeks at 37°C in an  
536 incubator with 5% CO<sub>2</sub>.

537

538 **Transportation of Transwells containing airway epithelia.** The differentiated airway epithelia  
539 for 22 days were transported in transportation medium at 4°C via overnight FedEx biological  
540 material shipment to the Rocky Mountain Laboratories (RML, Hamilton, MT, USA). The  
541 semisolid transportation medium was prepared by adding agarose to the complete AEC medium.  
542 Upon receipt, the Transwells containing airway epithelia were immediately transferred into new  
543 plates with complete AEC medium in the basal part and maintained before infection as described  
544 in the section on ALI culture.

545

546 **Virus infection.** Virus infection was conducted in the high biocontainment facilities at RML,  
547 NIAID, NIH. The 4-week-differentiated airway epithelia were washed with 200 µl of 1x PBS to  
548 remove mucus and infected on the apical site with SARS-CoV-2 at an MOI of 0.1 in 1x PBS for  
549 1 hour (at 37°C with 5% CO<sub>2</sub>). For mock infection, the assigned Transwells were similarly  
550 incubated with 1x PBS without virus. The viral inoculum was then removed, and the epithelia  
551 were washed twice with 200 µl of 1x PBS. Two hundred microliters of apical wash and basal  
552 medium were collected for virus titration. Fresh ALI medium (1000 µl) with supplements was  
553 added to the basal part of each Transwell, and the apical part was kept empty. Mock-infected and

554 SARS-CoV-2-infected Transwells were incubated for 4 days at 37°C in an incubator with 5%  
555 CO<sub>2</sub>.

556

557 **Tissue culture infective dose 50 (TCID<sub>50</sub>).** Vero cells were seeded on 96-well plates to  
558 confluency, and SARS-CoV-2 endpoint titration was performed. The cells were inoculated with  
559 10-fold dilutions of the supernatants collected during the experiment in DMEM, 2% FBS, L-  
560 glutamine and P/S. The cells were incubated for 7 days, and the cytopathic effect (CPE) was  
561 scored under a microscope. The TCID<sub>50</sub> was calculated using the Reed-Muench formula (Reed  
562 and Muench, 1938).

563

564 **Virus-infected sample collection.** At 4 DPI, 200 µl of 1x PBS was added to the apical site of  
565 the Transwell and incubated for several minutes, and the apical wash was collected for virus  
566 titration. Similarly, basal medium was collected for virus titration. All the samples were stored at  
567 -80°C until titration. For PFA fixation, 200 µl of 4% PFA was added at the apical site of the  
568 Transwells and incubated for 30 minutes, and the Transwells were further maintained overnight  
569 in 4% PFA before being transported outside of the BSL4 lab according to the standard protocol  
570 of RML. For protein and RNA sample collections, 200 µl of 1x PBS was added to the apical side  
571 of each Transwell, and cells were scrapped with a mini scrapper, collected into a cryovial, and  
572 pelleted by being spun down with a table-top bench centrifuge. For the protein samples, 100 µl  
573 of 2x SDS buffer was added to the cryovials containing the cell pellet, and the tube was boiled  
574 for 10 minutes. After a quick spin, the samples were transferred into new tubes and removed  
575 from the BSL4 laboratory using a standard RML protocol. For the RNA samples, the cell pellets  
576 were resuspended in 600 µl of RLT buffer (Qiagen) and transported out of the laboratory based

577 on the RML protocol with 600 µl of ethanol. RNA was extracted using a Qiagen RNeasy mini  
578 kit (QIAGEN) and eluted in 50 µl of RNase-free water. All the samples were shipped to Mehedi  
579 Lab at UND using an appropriate overnight biological shipment procedure.

580

581 **Hematoxylin and eosin (H&E) staining.** Four days post infection, NHBE-ALI and COPD-ALI  
582 mock and infected Transwells were fixed with 4% PFA for 24 hours. The membrane was cut off  
583 using a scalpel and embedded in paraffin mold. Five-micrometer sections were cut using a  
584 microtome. H&E staining was performed by two 5-minute Histo-Clear incubations followed by  
585 three 5-minute incubations with 100% ethanol, one 5-minute incubation with 95% ethanol and  
586 one 5-minute incubation with 70% ethanol. Subsequently, the samples were washed with tap  
587 water for 2 minutes, incubated with 4% acidified Harries Hematoxylin for 2 minutes, washed  
588 with tap water for 2 minutes, and incubated with 0.5% lithium carbonate for 20 seconds. The  
589 samples were subsequently washed with tap water for 5 minutes, incubated with Eosin Y  
590 Solution with Phloxine for 2 minutes and then subjected to a series of ethanol incubations:  
591 incubation with 70% ethanol for 5 minutes, incubation with 95% ethanol for 5 minutes and three  
592 5-minutes incubation with 100% ethanol. Finally, two 5-minute incubations with Histo-Clear  
593 were performed, and coverslips were then placed using permanent mounting medium.

594

595 **Alcian blue staining.** The 5-µm sectioned ALI-NHBE and COPD mock and infected samples  
596 were also subjected to Alcian blue staining. The sections were deparaffinized as described in the  
597 section on H&E staining using Histo-Clear and ethanol. The cells were then washed with tap  
598 water for 2 minutes, incubated in 3% acetic acid for 3 minutes and stained with Alcian blue for  
599 30 minutes. The sections were subsequently rinsed with 3% acetic acid for 10 seconds to help

600 prevent nonspecific staining. The sections were washed under tap water for 10 minutes and then  
601 rinsed for 2 minutes in Milli-Q water. The sections were counterstained with nuclear fast red  
602 solution for 5 minutes and washed under tap water for 5 minutes. The sections were subsequently  
603 dehydrated and cleared with a gradient of alcohol and Histo-Clear as in the protocol used for  
604 H&E staining. The slides were mounted with permanent mounting medium and coverslipped.

605

606 **Fluorescence imaging.** The apical site of the airway epithelium was washed with PBS, and both  
607 the apical and basal parts were fixed with 4% paraformaldehyde (PFA) (Polysciences, Inc.), and  
608 blocked with 10% goat serum (Vector Laboratories) solution in immunofluorescence (IF)  
609 washing buffer (130 mM NaCl<sub>2</sub>, 7 mM Na<sub>2</sub>HPO<sub>4</sub>, 3.5 mM NaH<sub>2</sub>PO<sub>4</sub>, 7.7 mM NaN<sub>3</sub>, 0.1% BSA,  
610 0.2% Triton-X 100 and 0.05% Tween-20) for 1 hour. The Transwell inserts were then incubated  
611 with the following primary antibodies (Abs) (alone or in combination) in IF washing buffer  
612 overnight at 4°C: anti-ZO-1 rabbit polyclonal (1:200) (Thermo Fisher Scientific), anti-E-  
613 cadherin rabbit monoclonal (1:200) (Cell Signaling Technologies), anti-MUC5B rabbit  
614 monoclonal (1:500) (Atlas Antibodies), anti-MUC5AC mouse polyclonal (1:100) (Abnova),  
615 anti-MUC5AC rabbit monoclonal (1:200) (Cell Signaling Technology), anti-acetyl-alpha-tubulin  
616 rabbit monoclonal (1:500) (Cell Signaling Technologies), anti-TMPRSS2 mouse monoclonal  
617 (1:50) (Santa Cruz Biotechnology), anti-SARS CoV-2 nucleocapsid mouse monoclonal (1:10)  
618 (Thermo Fisher Scientific) and anti-ACE2 mouse monoclonal (1:20) (R&D Systems). The next  
619 day, the inserts were washed with the IF washing buffer and incubated with an anti-mouse  
620 AlexaFlour 488-conjugated Ab (1:200) (Thermo Fisher Scientific) and/or an anti-rabbit  
621 AlexaFlour 647 (1:200) (Thermo Fisher Scientific) in IF washing buffer for 3 hours in the dark at  
622 4°C. The cells were washed twice with PBS and incubated with rhodamine phalloidin (1:500)

623 (Cytoskeleton Inc.) in IF washing buffer for 30 minutes at room temperature in the dark. After  
624 two washes with PBS, the cell nuclei were stained with NucBlue Fixed Cell Stain ReadyProbes  
625 (Thermo Fisher Scientific) for 30 minutes in the dark at room temperature. The epithelium was  
626 mounted on Tech-Med microscope slides (Thomas Scientific) using ProLong-Gold anti-fade  
627 mounting medium (Thermo Fisher Scientific). Images were captured using a confocal laser-  
628 scanning microscope (Olympus FV3000) enabled with a 60X objective. The 405-nm laser was  
629 used to excite the DAPI signal for nucleus detection, the 488-nm laser was used to excite Alexa  
630 Flour 488 for MUC5AC, ACE2, TMPRSS2 or SARS CoV-2 nucleocapsid protein detection, the  
631 561-nm laser was used to excite rhodamine phalloidin for F-actin detection, and the 640-nm laser  
632 was used to excite Alexa Flour 647 for MUC5B, acetyl-alpha-tubulin, E-cadherin, ZO-1 or  
633 MUC5AC detection. At least two random fields were selected per sample and imaged. The  
634 images were processed with Imaris software version 9.5.1 (Oxford Instruments Group) and used  
635 for the conversion of Z-stack images (.oir format) to .tiff format and for additional image  
636 postprocessing. Separately, the tiling of Z-stack (3x3) images was captured using a Leica DMI8  
637 microscope followed by image processing using a 3D deconvolution image processing module in  
638 the LASX software (Leica Microsystem) associated with the microscope. We used nine  
639 independent images to quantify the total cell number based on F-actin (Texas Red channel) and  
640 goblet cells using the Alexa Flour 647 channel (anti-MUC5B) with the Fiji multipointer option.  
641 Similarly, we quantified the MUC5AC<sup>+</sup> cells using at least two confocal images.

642

643 **Immunohistochemistry:** Healthy and COPD airway epithelia (mock or infected) were sectioned  
644 into 5- $\mu$ m sections as described previously for immunohistochemistry. Before staining, the  
645 antigen retrieval process was performed using R-buffer A in a Retriever 2100. The slides were

646 allowed to cool in the buffer overnight and washed three times in PBST (0.05% Tween-20) for  
647 10 minutes. Using a Pap pen, a hydrophobic barrier was drawn around the tissue. Once the  
648 hydrophobic barrier was dry, the tissue was incubated with blocking buffer (10% goat serum in  
649 PBS) for 2 hours in a humidified, light-protected chamber. After incubation with blocking buffer,  
650 the tissue was immediately incubated with the following primary antibodies overnight at 4°C in a  
651 humidified, light-protected chamber: SARS-CoV-2 N (1:50) (Thermo Fischer Scientific) for the  
652 detection of SARS-CoV-2 nucleoprotein (N), SARS-CoV-2 spike (S) protein (1:100) (Thermo  
653 Fischer Scientific) for the detection of SARS-CoV2 S protein, acetylated-alpha-tubulin (1:500)  
654 (Cell Signaling Technologies) for the staining of ciliated cells, MUC5AC (1:500) (Cell Signaling  
655 Technologies) and MUC5B (1:500) (Atlas Antibodies) for the staining of goblet cells, and P63  
656 (1:100) (Abcam Inc.) for the staining of basal cells. The next day, the slides were washed three  
657 times with PBST and then incubated for 45 minutes with anti-mouse Alexa Fluor 488 (Thermo  
658 Fisher Scientific) and anti-rabbit Alexa Fluor 647 (Thermo Fisher Scientific) secondary  
659 antibodies in a humidified, light-protected chamber. The slides were subsequently washed three  
660 times with PBST, incubated with rhodamine phalloidin (1:100) (Cytoskeleton Inc.) for 30  
661 minutes at room temperature in a humidified, light-protected chamber, and washed three times  
662 with PBST. The nuclei were then stained by incubation with NucBlue Fixed Cell Stain  
663 ReadyProbes (Thermo Fisher Scientific) for 5 minutes at room temperature in a humidified,  
664 light-protected chamber. After incubation with the nuclear dye, the slides were washed once with  
665 PBST and twice with DI water, and coverglass was then placed on the tissue section using  
666 ProLong-Gold anti-fade mounting medium (Thermo Fisher Scientific). The slides were scanned  
667 using a Leica DMI8 inverted fluorescence microscope with a 63X oil objective, and the images

668 were further processed using a 3D deconvolution image processing module in the LASX  
669 software (Leica Microsystem) associated with the microscope.

670

671 **Ciliary beat frequency (CBF).** Cilia on the apical surface of the cells in the differentiated  
672 epithelial layer (after 4 weeks of differentiation) were visualized in the phase-contrast mode with  
673 a Leica DMI8 microscope with a 20X objective and an attached environment control chamber  
674 (37°C with 5% CO<sub>2</sub>) (Leica Microsystems). For each Transwell, six different random fields were  
675 recorded for approximately 2.1 seconds at 120 frames per second. The images were captured at  
676 37°C and analyzed using the Sisson-Ammons Video Analysis (SAVA) system V.2.1.15 to  
677 determine the CBF (Hz) (Ammons Engineering).

678

679 **Transepithelial electrical resistance (TEER).** The permeability of the differentiated epithelial  
680 layer (after 4 weeks of differentiation) was determined by measuring the TEER using an  
681 epithelial volt-ohm meter (EVOM2, World Precision Instruments, Inc.). The EVOM2 was  
682 calibrated according to the manufacturer's instructions, and the STX2 electrode was sterilized  
683 with 70% ethanol before use. The internal electrode (smaller in size) was placed in the apical  
684 part of each Transwell (PBS was added during the TEER reading), and the external electrode  
685 (larger in size) was placed in the basal part of the Transwell, which contained ALI basal medium,  
686 to measure the membrane voltage and resistance of the epithelial layer. An empty Transwell  
687 insert (filled with PBS) containing no NHBE cells was used to correct for the background  
688 resistance. Three readings were taken for each Transwell. The TEER value of each sample was  
689 calculated by subtracting the background value.

690

691 **Quantitative real-time PCR.** Airway epithelia cultured on 6.5-mm Transwell membranes were  
692 washed and treated for 1 minute at RT with RLT buffer (Qiagen) with 1%  $\beta$ -mercaptoethanol  
693 (Sigma-Aldrich). The cells were scraped using a cell scraper, collected into a QIAshredder tube  
694 and centrifuged at 15,000 rpm and 4°C for 3 minutes. The eluate was used for the extraction of  
695 total RNA using a Total DNA/RNA Extraction Kit (Qiagen), and DNase I treatment was  
696 performed to remove DNA from the samples according to the manufacturer's instructions. We  
697 also followed a similar approach for the extraction of RNA from A549 cells. The RNA  
698 concentration was determined with an Epoch microplate spectrophotometer (BioTek). Five  
699 hundred nanograms of RNA was used for first-strand cDNA synthesis (Thermo Fisher Scientific)  
700 using Oligo(dT) primers (Thermo Fisher Scientific). qRT-PCR was performed using TaqMan  
701 assays (ACE2: Hs1085333\_m1 and ACTB: Hs99999903\_m1, for calibration) (Thermo Fisher  
702 Scientific) with the CFX384 Real-Time PCR System (Bio-Rad), and fold changes were  
703 calculated to determine the relative expression levels.

704  
705 **Western blotting.** The airway epithelium cultured on 6.5-mm Transwell membranes was  
706 washed with PBS, scraped out of all the cells, and pelleted by centrifugation at 10,000 rpm for 5  
707 minutes. The cell pellet was incubated with 1x LDS loading buffer (Thermo Fisher Scientific)  
708 with proteinase inhibitor (Roche), transferred into a QIAshredder microcentrifuge tube, and  
709 centrifuged for 3 minutes at 15,000 rpm in a tabletop centrifuge. The elution from the  
710 QIAshredder was collected and stored in a freezer. The protein concentration was measured  
711 using a BCA protein assay kit (Thermo Fisher Scientific). For the detection of ACE2, total  
712 protein (30  $\mu$ g) was separated on 4-12% Bis-tris SDS polyacrylamide gels (reducing) and then  
713 subjected to dry blot transfer onto PVDF membranes according to the manufacturer's instructions

714 (Life Technologies). The PVDF membrane was imaged using an Odyssey CLX system (Li-Cor  
715 Biosciences). ACE2 was detected by Western blotting using anti-ACE2 goat polyclonal antibody  
716 (R&D Systems) and corresponding donkey anti-goat IRDye 800 secondary antibodies (Li-Cor  
717 Biosciences). For the loading control, alpha-tubulin was detected by anti-alpha-tubulin mouse  
718 monoclonal antibody (Sigma-Aldrich) and the corresponding goat anti-mouse IRDye 680  
719 secondary antibody (Li-Cor Biosciences). Image Studio 5.2 (LI-COR Biosciences) was used to  
720 quantify the protein signal.

721

722 **Epithelial height measurement.** Microscopic images of the IHC (described above) were used to  
723 quantify epithelial height by using the scale feature in LASX software of Leica DMI8  
724 microscope. We used at least 4 independent slides for the measurement, at least three  
725 independent reads per slide. The plastic membrane of the Transwell was not included in the  
726 height measurement.

727

## 728 **QUANTIFICATION AND STATISTICAL ANALYSIS**

729

730 **Statistical analysis:** Parameters such as the number of replicates, number of independent  
731 experiments, mean +/- SEM, and statistical significance are reported in the figures and figure  
732 legends. A p-value less than 0.05 was considered to indicate significance. Where appropriate, the  
733 statistical tests and post hoc statistical analysis methods are noted in the figure legends or  
734 Methods section.

735

736 **References.**

737 Araya, J., Cambier, S., Markovics, J.A., Wolters, P., Jablons, D., Hill, A., Finkbeiner, W., Jones, K., Broaddus,  
738 V.C., Sheppard, D., *et al.* (2007). Squamous metaplasia amplifies pathologic epithelial-mesenchymal interactions in  
739 COPD patients. *J Clin Invest* *117*, 3551-3562.

740 Barnes, P.J. (2013). New anti-inflammatory targets for chronic obstructive pulmonary disease. *Nat Rev Drug Discov*  
741 *12*, 543-559.

742 Blanco-Melo, D., Nilsson-Payant, B.E., Liu, W.C., Uhl, S., Hoagland, D., Moller, R., Jordan, T.X., Oishi, K., Panis,  
743 M., Sachs, D., *et al.* (2020). Imbalanced Host Response to SARS-CoV-2 Drives Development of COVID-19. *Cell*.

744 Borczuk, A.C., Salvatore, S.P., Seshan, S.V., Patel, S.S., Bussel, J.B., Mostyka, M., Elsoukkary, S., He, B., Del  
745 Vecchio, C., Fortarezza, F., *et al.* (2020). COVID-19 pulmonary pathology: a multi-institutional autopsy cohort  
746 from Italy and New York City. *Mod Pathol*.

747 Bradley, B.T., Maioli, H., Johnston, R., Chaudhry, I., Fink, S.L., Xu, H., Najafian, B., Deutsch, G., Lacy, J.M.,  
748 Williams, T., *et al.* (2020). Histopathology and ultrastructural findings of fatal COVID-19 infections in Washington  
749 State: a case series. *Lancet* *396*, 320-332.

750 Brusselle, G.G., Joos, G.F., and Bracke, K.R. (2011). New insights into the immunology of chronic obstructive  
751 pulmonary disease. *Lancet* *378*, 1015-1026.

752 CDC (2020). People with Certain Medical Conditions (CDC).

753 Coutard, B., Valle, C., de Lamballerie, X., Canard, B., Seidah, N.G., and Decroly, E. (2020). The spike glycoprotein  
754 of the new coronavirus 2019-nCoV contains a furin-like cleavage site absent in CoV of the same clade. *Antiviral*  
755 *Res* *176*, 104742.

756 Crystal, R.G. (2014). Airway basal cells. The "smoking gun" of chronic obstructive pulmonary disease. *Am J Respir*  
757 *Crit Care Med* *190*, 1355-1362.

758 Dhand, R., and Li, J. (2020). Coughs and Sneezes: Their Role in Transmission of Respiratory Viral Infections,  
759 Including SARS-CoV-2. *Am J Respir Crit Care Med* *202*, 651-659.

760 Falasca, L., Nardacci, R., Colombo, D., Lalle, E., Di Caro, A., Nicastrì, E., Antinori, A., Petrosillo, N., Marchioni,  
761 L., Biava, G., *et al.* (2020). Post-Mortem Findings in Italian Patients with COVID-19 - a Descriptive Full Autopsy  
762 Study of cases with and without co-morbidities. *J Infect Dis*.

763 Franks, T.J., Chong, P.Y., Chui, P., Galvin, J.R., Lourens, R.M., Reid, A.H., Selbs, E., McEvoy, C.P., Hayden,  
764 C.D., Fukuoka, J., *et al.* (2003). Lung pathology of severe acute respiratory syndrome (SARS): a study of 8 autopsy  
765 cases from Singapore. *Hum Pathol* *34*, 743-748.

766 Fulcher, M.L., Gabriel, S., Burns, K.A., Yankaskas, J.R., and Randell, S.H. (2005). Well-differentiated human  
767 airway epithelial cell cultures. *Methods Mol Med* *107*, 183-206.

768 Giacca, M., Bussani, R., Schneider, E., Zentilin, L., Collesi, C., Ali, H., Braga, L., Secco, I., Volpe, M.C., and  
769 Colliva, A. (2020). Persistence of viral RNA, widespread thrombosis and abnormal cellular syncytia are hallmarks  
770 of COVID-19 lung pathology. medRxiv.

771 Gohy, S., Carlier, F.M., Fregimilicka, C., Detry, B., Lecocq, M., Ladjemi, M.Z., Verleden, S., Hoton, D., Weynand,  
772 B., Bouzin, C., *et al.* (2019). Altered generation of ciliated cells in chronic obstructive pulmonary disease. *Sci Rep* *9*,  
773 17963.

774 Guan, W.J., Ni, Z.Y., Hu, Y., Liang, W.H., Ou, C.Q., He, J.X., Liu, L., Shan, H., Lei, C.L., Hui, D.S.C., *et al.*  
775 (2020). Clinical Characteristics of Coronavirus Disease 2019 in China. *N Engl J Med* *382*, 1708-1720.

776 Hamming, I., Timens, W., Bulthuis, M.L., Lely, A.T., Navis, G., and van Goor, H. (2004). Tissue distribution of  
777 ACE2 protein, the functional receptor for SARS coronavirus. A first step in understanding SARS pathogenesis. *J*  
778 *Pathol* *203*, 631-637.

779 Hao, S., Ning, K., Kuz, C.A., Vorhies, K., Yan, Z., and Qiu, J. (2020). Long-Term Modeling of SARS-CoV-2  
780 Infection of In Vitro Cultured Polarized Human Airway Epithelium. *mBio* *11*.

781 Harcourt, J., Tamin, A., Lu, X., Kamili, S., Sakthivel, S.K., Murray, J., Queen, K., Tao, Y., Paden, C.R., Zhang, J.,  
782 *et al.* (2020). Severe Acute Respiratory Syndrome Coronavirus 2 from Patient with Coronavirus Disease, United  
783 States. *Emerg Infect Dis* *26*, 1266-1273.

784 Higham, A., Quinn, A.M., Cancado, J.E.D., and Singh, D. (2019). The pathology of small airways disease in COPD:  
785 historical aspects and future directions. *Respir Res* *20*, 49.

786 Hoffmann, M., Kleine-Weber, H., Schroeder, S., Kruger, N., Herrler, T., Erichsen, S., Schiergens, T.S., Herrler, G.,  
787 Wu, N.H., Nitsche, A., *et al.* (2020). SARS-CoV-2 Cell Entry Depends on ACE2 and TMPRSS2 and Is Blocked by  
788 a Clinically Proven Protease Inhibitor. *Cell* *181*, 271-280 e278.

789 Hou, Y.J., Okuda, K., Edwards, C.E., Martinez, D.R., Asakura, T., Dinnon, K.H., 3rd, Kato, T., Lee, R.E., Yount,  
790 B.L., Mascenik, T.M., *et al.* (2020). SARS-CoV-2 Reverse Genetics Reveals a Variable Infection Gradient in the  
791 Respiratory Tract. *Cell* *182*, 429-446 e414.

792 Huang, C., Wang, Y., Li, X., Ren, L., Zhao, J., Hu, Y., Zhang, L., Fan, G., Xu, J., Gu, X., *et al.* (2020). Clinical  
793 features of patients infected with 2019 novel coronavirus in Wuhan, China. *Lancet* 395, 497-506.

794 Jia, H.P., Look, D.C., Hickey, M., Shi, L., Pewe, L., Netland, J., Farzan, M., Wohlford-Lenane, C., Perlman, S., and  
795 McCray, P.B., Jr. (2006). Infection of human airway epithelia by SARS coronavirus is associated with ACE2  
796 expression and localization. *Adv Exp Med Biol* 581, 479-484.

797 Jia, H.P., Look, D.C., Shi, L., Hickey, M., Pewe, L., Netland, J., Farzan, M., Wohlford-Lenane, C., Perlman, S., and  
798 McCray, P.B., Jr. (2005). ACE2 receptor expression and severe acute respiratory syndrome coronavirus infection  
799 depend on differentiation of human airway epithelia. *J Virol* 79, 14614-14621.

800 Kim, V., Oros, M., Durra, H., Kelsen, S., Aksoy, M., Cornwell, W.D., Rogers, T.J., and Criner, G.J. (2015). Chronic  
801 bronchitis and current smoking are associated with more goblet cells in moderate to severe COPD and smokers  
802 without airflow obstruction. *PLoS One* 10, e0116108.

803 Kiyokawa, H., and Morimoto, M. (2020). Notch signaling in the mammalian respiratory system, specifically the  
804 trachea and lungs, in development, homeostasis, regeneration, and disease. *Dev Growth Differ* 62, 67-79.

805 Lamers, M.M., Beumer, J., van der Vaart, J., Knoops, K., Puschhof, J., Breugem, T.I., Ravelli, R.B.G., Paul van  
806 Schayck, J., Mykytyn, A.Z., Duimel, H.Q., *et al.* (2020). SARS-CoV-2 productively infects human gut enterocytes.  
807 *Science* 369, 50-54.

808 Leung, J.M., Niikura, M., Yang, C.W.T., and Sin, D.D. (2020). COVID-19 and COPD. *Eur Respir J* 56.

809 Li, M.Y., Li, L., Zhang, Y., and Wang, X.S. (2020). Expression of the SARS-CoV-2 cell receptor gene ACE2 in a  
810 wide variety of human tissues. *Infect Dis Poverty* 9, 45.

811 Li, W., Moore, M.J., Vasilieva, N., Sui, J., Wong, S.K., Berne, M.A., Somasundaran, M., Sullivan, J.L., Luzuriaga,  
812 K., Greenough, T.C., *et al.* (2003). Angiotensin-converting enzyme 2 is a functional receptor for the SARS  
813 coronavirus. *Nature* 426, 450-454.

814 Lippi, G., and Henry, B.M. (2020). Chronic obstructive pulmonary disease is associated with severe coronavirus  
815 disease 2019 (COVID-19). *Respir Med* 167, 105941.

816 Lukassen, S., Chua, R.L., Trefzer, T., Kahn, N.C., Schneider, M.A., Muley, T., Winter, H., Meister, M., Veith, C.,  
817 Boots, A.W., *et al.* (2020). SARS-CoV-2 receptor ACE2 and TMPRSS2 are primarily expressed in bronchial  
818 transient secretory cells. *EMBO J* 39, e105114.

819 Martinez, R.B., Ritter, J.M., Matkovic, E., Gary, J., Bollweg, B.C., Bullock, H., Goldsmith, C.S., Silva-Flannery, L.,  
820 Seixas, J.N., Reagan-Steiner, S., *et al.* (2020). Pathology and Pathogenesis of SARS-CoV-2 Associated with Fatal  
821 Coronavirus Disease, United States. *Emerg Infect Dis* 26, 2005-2015.

822 Matrosovich, M.N., Matrosovich, T.Y., Gray, T., Roberts, N.A., and Klenk, H.D. (2004). Human and avian  
823 influenza viruses target different cell types in cultures of human airway epithelium. *Proc Natl Acad Sci U S A* 101,  
824 4620-4624.

825 Okuda, K., Chen, G., Subramani, D.B., Wolf, M., Gilmore, R.C., Kato, T., Radicioni, G., Kesimer, M., Chua, M.,  
826 Dang, H., *et al.* (2019). Localization of Secretory Mucins MUC5AC and MUC5B in Normal/Healthy Human  
827 Airways. *Am J Respir Crit Care Med* 199, 715-727.

828 Pawlina, W. (2016). In *Histology a Text Book and Atlas with Correlated Cell and Molecular Biology*, W. Pawlina,  
829 ed. (Wolters Kluwer), pp. 671-697.

830 Persson, B.D., Jaffe, A.B., Fearn, R., and Danahay, H. (2014). Respiratory syncytial virus can infect basal cells and  
831 alter human airway epithelial differentiation. *PLoS One* 9, e102368.

832 Polosukhin, V.V., Cates, J.M., Lawson, W.E., Zaynagetdinov, R., Milstone, A.P., Massion, P.P., Ocak, S., Ware,  
833 L.B., Lee, J.W., Bowler, R.P., *et al.* (2011). Bronchial secretory immunoglobulin a deficiency correlates with airway  
834 inflammation and progression of chronic obstructive pulmonary disease. *Am J Respir Crit Care Med* 184, 317-327.

835 Qi, F., Qian, S., Zhang, S., and Zhang, Z. (2020). Single cell RNA sequencing of 13 human tissues identify cell  
836 types and receptors of human coronaviruses. *Biochem Biophys Res Commun* 526, 135-140.

837 Randell, S.H. (2006). Airway epithelial stem cells and the pathophysiology of chronic obstructive pulmonary  
838 disease. *Proc Am Thorac Soc* 3, 718-725.

839 Rayner, R.E., Makena, P., Prasad, G.L., and Cormet-Boyaka, E. (2019). Optimization of Normal Human Bronchial  
840 Epithelial (NHBE) Cell 3D Cultures for in vitro Lung Model Studies. *Sci Rep* 9, 500.

841 Reed, L.J., and Muench, H. (1938). A simple method of estimating fifty per cent endpoints. *American journal of*  
842 *epidemiology* 27, 493-497.

843 Reid, A.T., Veerati, P.C., Gosens, R., Bartlett, N.W., Wark, P.A., Grainge, C.L., Stick, S.M., Kicic, A., Moheimani,  
844 F., Hansbro, P.M., *et al.* (2018). Persistent induction of goblet cell differentiation in the airways: Therapeutic  
845 approaches. *Pharmacol Ther* 185, 155-169.

846 Rigden, H.M., Alias, A., Havelock, T., O'Donnell, R., Djukanovic, R., Davies, D.E., and Wilson, S.J. (2016).  
847 Squamous Metaplasia Is Increased in the Bronchial Epithelium of Smokers with Chronic Obstructive Pulmonary  
848 Disease. *PLoS One* 11, e0156009.

849 Rogers, D.F. (2003). The airway goblet cell. *Int J Biochem Cell Biol* 35, 1-6.

850 Schaefer, I.M., Padera, R.F., Solomon, I.H., Kanjilal, S., Hammer, M.M., Hornick, J.L., and Sholl, L.M. (2020). In  
851 situ detection of SARS-CoV-2 in lungs and airways of patients with COVID-19. *Mod Pathol* 33, 2104-2114.

852 Shaykhiiev, R. (2019). Emerging biology of persistent mucous cell hyperplasia in COPD. *Thorax* 74, 4-6.

853 Shimura, S., Andoh, Y., Haraguchi, M., and Shirato, K. (1996). Continuity of airway goblet cells and intraluminal  
854 mucus in the airways of patients with bronchial asthma. *Eur Respir J* 9, 1395-1401.

855 Shulla, A., Heald-Sargent, T., Subramanya, G., Zhao, J., Perlman, S., and Gallagher, T. (2011). A transmembrane  
856 serine protease is linked to the severe acute respiratory syndrome coronavirus receptor and activates virus entry. *J*  
857 *Virology* 85, 873-882.

858 Sims, A.C., Baric, R.S., Yount, B., Burkett, S.E., Collins, P.L., and Pickles, R.J. (2005). Severe acute respiratory  
859 syndrome coronavirus infection of human ciliated airway epithelia: role of ciliated cells in viral spread in the  
860 conducting airways of the lungs. *J Virol* 79, 15511-15524.

861 Sin, D.D. (2020). COVID-19 in COPD: A growing concern. *EClinicalMedicine* 26, 100546.

862 Sungnak, W., Huang, N., Becavin, C., Berg, M., Queen, R., Litvinukova, M., Talavera-Lopez, C., Maatz, H.,  
863 Reichart, D., Sampaziotis, F., *et al.* (2020). SARS-CoV-2 entry factors are highly expressed in nasal epithelial cells  
864 together with innate immune genes. *Nat Med* 26, 681-687.

865 To, K.F., and Lo, A.W. (2004). Exploring the pathogenesis of severe acute respiratory syndrome (SARS): the tissue  
866 distribution of the coronavirus (SARS-CoV) and its putative receptor, angiotensin-converting enzyme 2 (ACE2). *J*  
867 *Pathol* 203, 740-743.

868 Wang, B.Y., Gil, J., Kaufman, D., Gan, L., Kohtz, D.S., and Burstein, D.E. (2002). P63 in pulmonary epithelium,  
869 pulmonary squamous neoplasms, and other pulmonary tumors. *Hum Pathol* 33, 921-926.

870 Wang, W., Xu, Y., Gao, R., Lu, R., Han, K., Wu, G., and Tan, W. (2020). Detection of SARS-CoV-2 in Different  
871 Types of Clinical Specimens. *JAMA*.

872 Whitsett, J.A. (2018). Airway Epithelial Differentiation and Mucociliary Clearance. *Ann Am Thorac Soc* 15, S143-  
873 S148.

874 Wolf, S., Perez, G.F., Mukharesh, L., Isaza, N., Preciado, D., Freishtat, R.J., Pillai, D., Rose, M.C., and Nino, G.  
875 (2017). Conditional reprogramming of pediatric airway epithelial cells: A new human model to investigate early-life  
876 respiratory disorders. *Pediatr Allergy Immunol* 28, 810-817.

877 Wolfel, R., Corman, V.M., Guggemos, W., Seilmaier, M., Zange, S., Muller, M.A., Niemeyer, D., Jones, T.C.,  
878 Vollmar, P., Rothe, C., *et al.* (2020). Virological assessment of hospitalized patients with COVID-2019. *Nature* 581,  
879 465-469.

880 Yang, X., Yu, Y., Xu, J., Shu, H., Xia, J., Liu, H., Wu, Y., Zhang, L., Yu, Z., Fang, M., *et al.* (2020). Clinical course  
881 and outcomes of critically ill patients with SARS-CoV-2 pneumonia in Wuhan, China: a single-centered,  
882 retrospective, observational study. *Lancet Respir Med* 8, 475-481.

883 Zhang, H., Rostami, M.R., Leopold, P.L., Mezey, J.G., O'Beirne, S.L., Strulovici-Barel, Y., and Crystal, R.G.  
884 (2020). Expression of the SARS-CoV-2 ACE2 Receptor in the Human Airway Epithelium. *Am J Respir Crit Care*  
885 *Med* 202, 219-229.

886 Zhang, L., Peeples, M.E., Boucher, R.C., Collins, P.L., and Pickles, R.J. (2002). Respiratory syncytial virus  
887 infection of human airway epithelial cells is polarized, specific to ciliated cells, and without obvious cytopathology.  
888 *J Virol* 76, 5654-5666.

889 Zhao, Q., Meng, M., Kumar, R., Wu, Y., Huang, J., Lian, N., Deng, Y., and Lin, S. (2020). The impact of COPD  
890 and smoking history on the severity of COVID-19: A systemic review and meta-analysis. *J Med Virol*.

891 Ziegler, C.G.K., Allon, S.J., Nyquist, S.K., Mbano, I.M., Miao, V.N., Tzouanas, C.N., Cao, Y., Yousif, A.S., Bals,  
892 J., Hauser, B.M., *et al.* (2020). SARS-CoV-2 Receptor ACE2 Is an Interferon-Stimulated Gene in Human Airway  
893 Epithelial Cells and Is Detected in Specific Cell Subsets across Tissues. *Cell*.

894

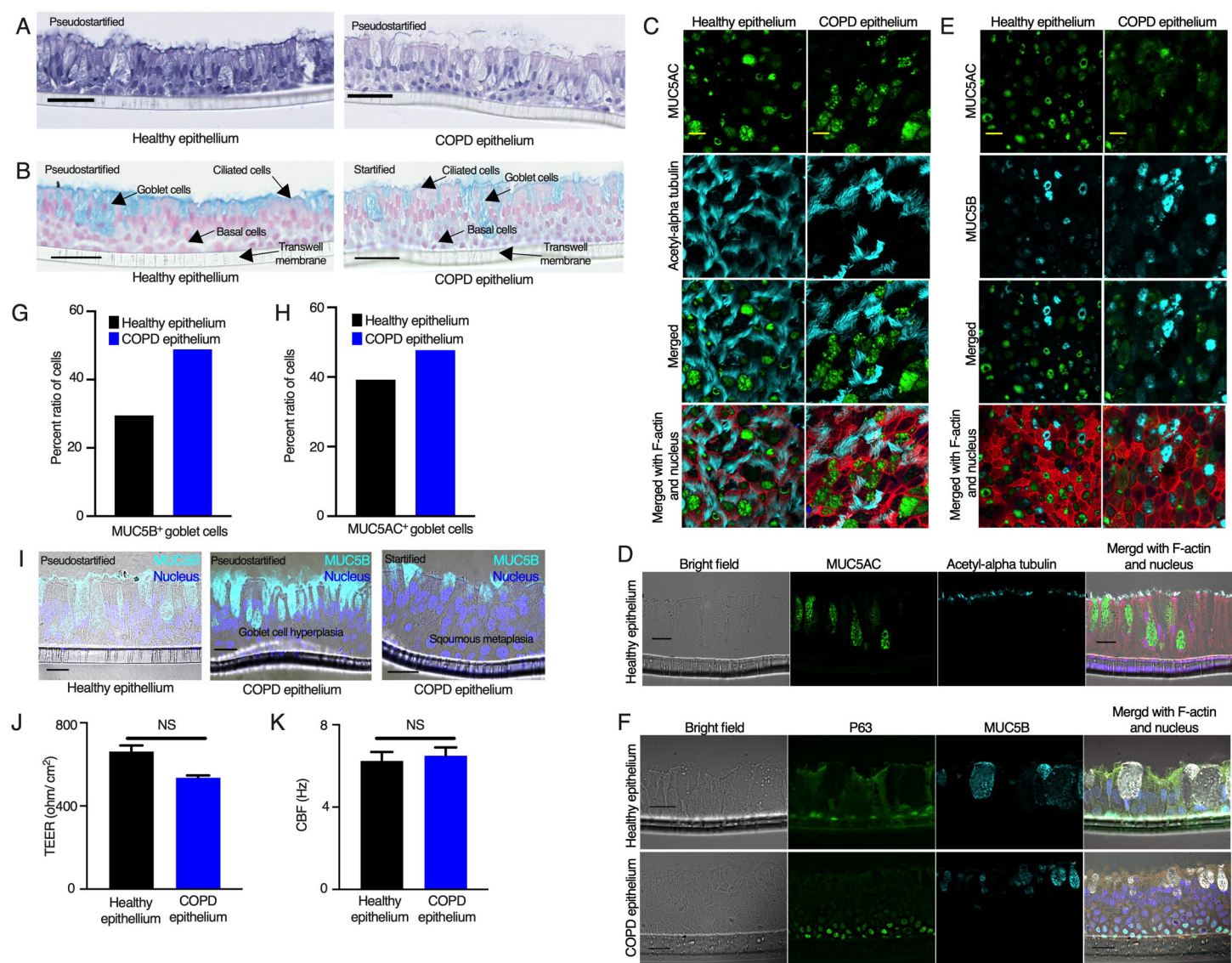


**Figure 1**

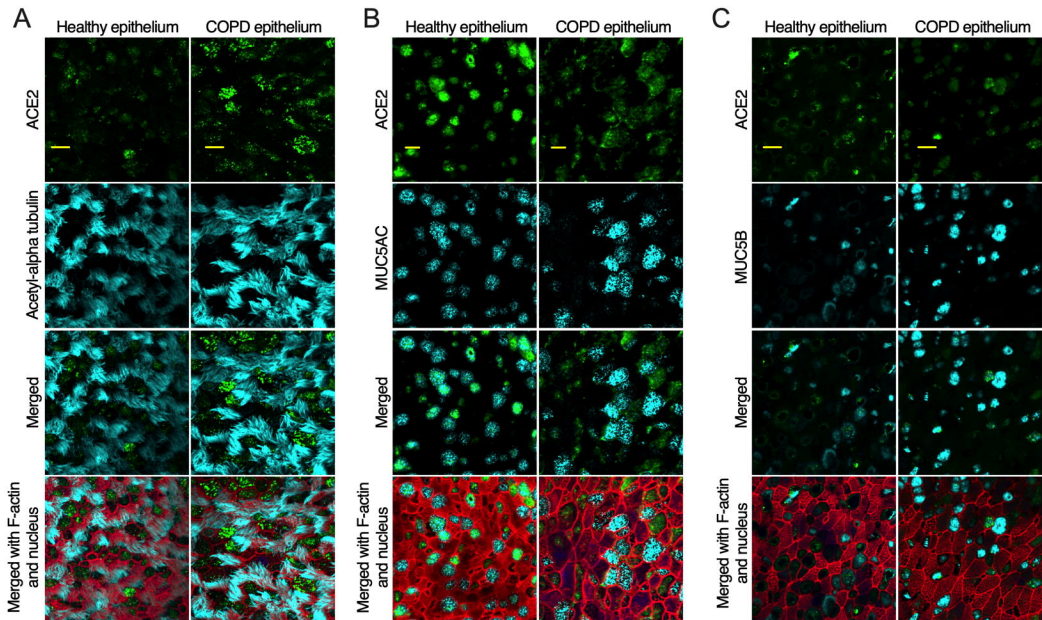


**Figure 2**

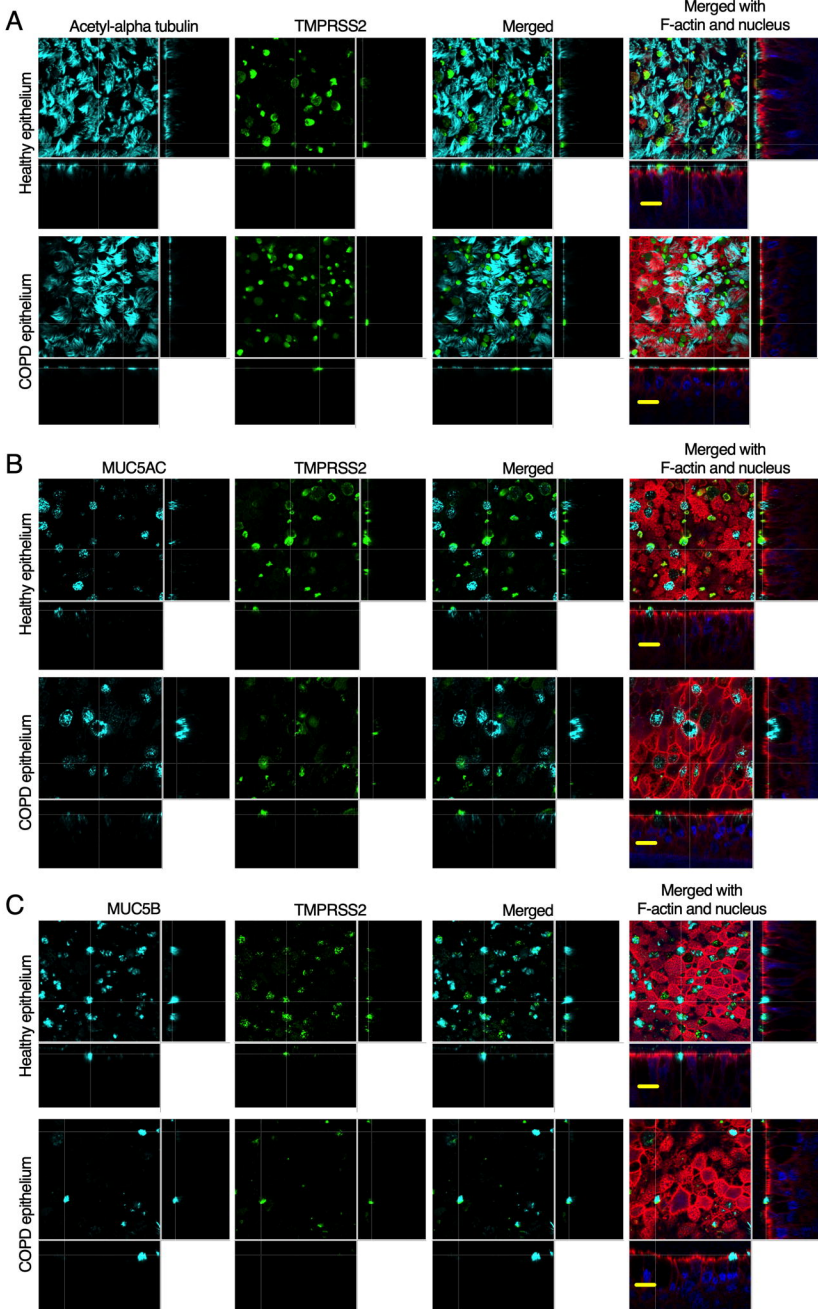


**Figure 3**

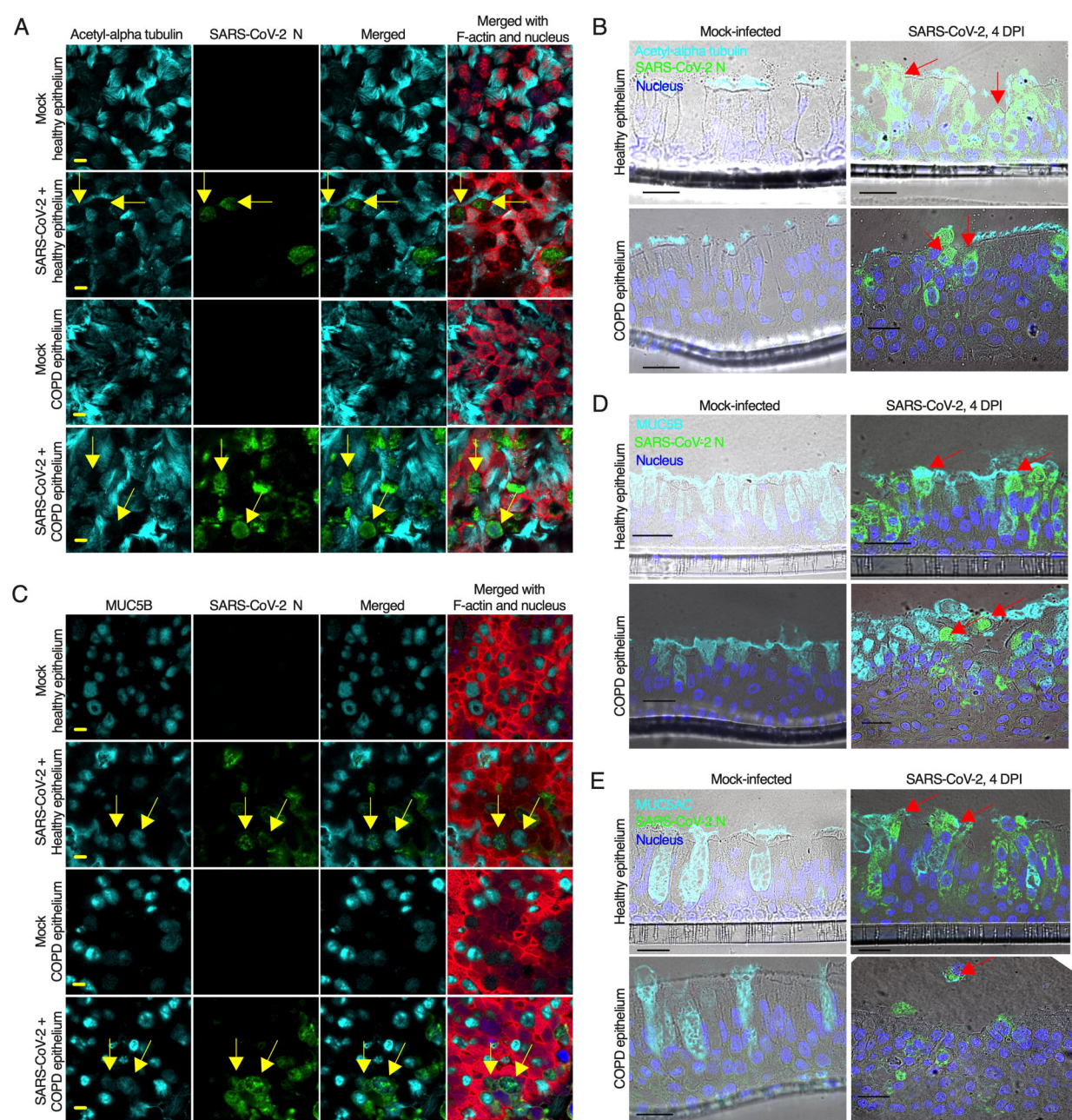


**Figure 4**

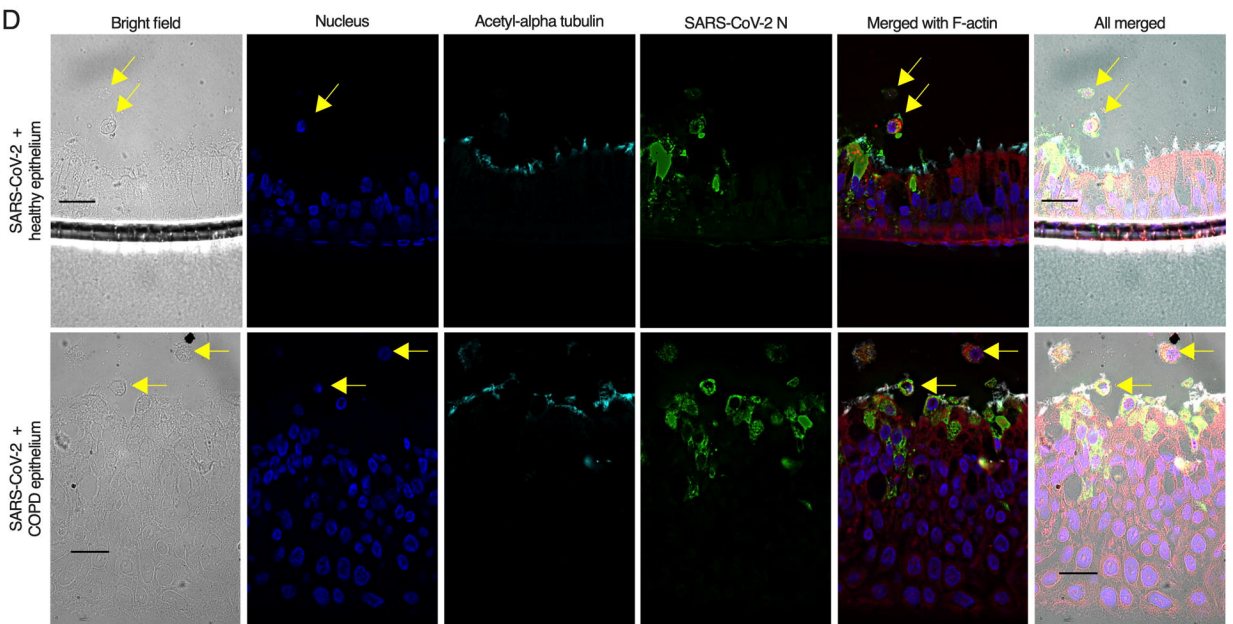
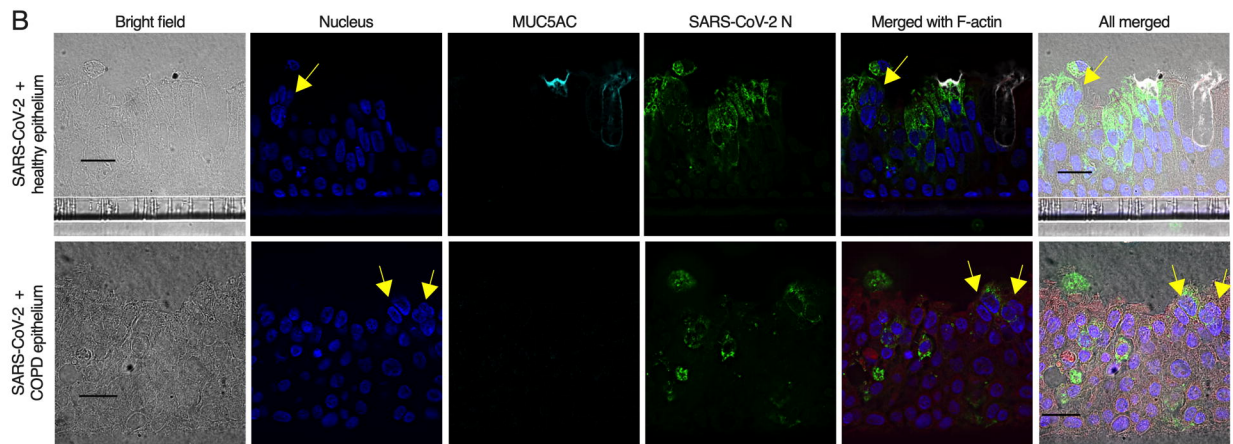
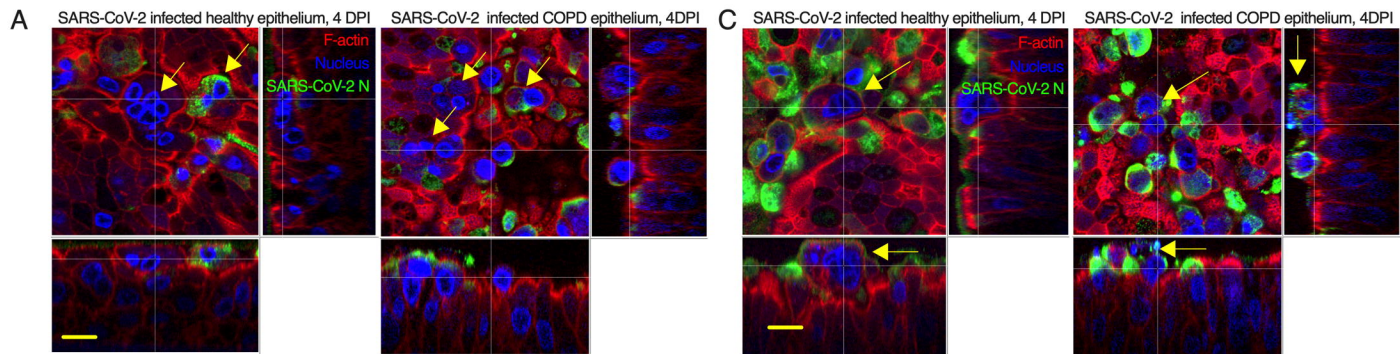


**Figure 5**

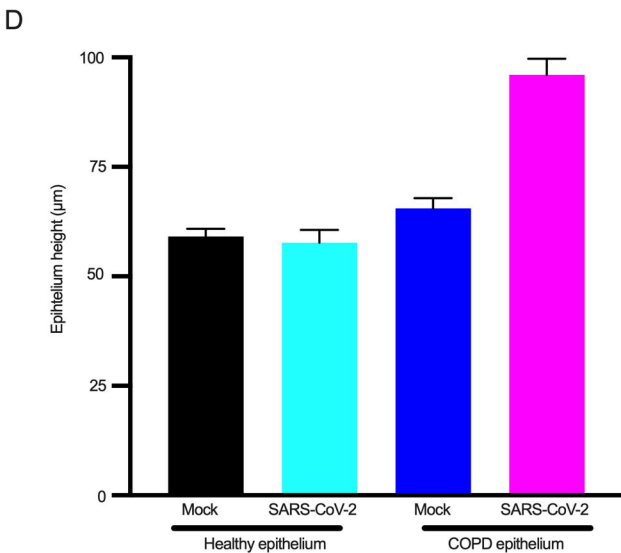
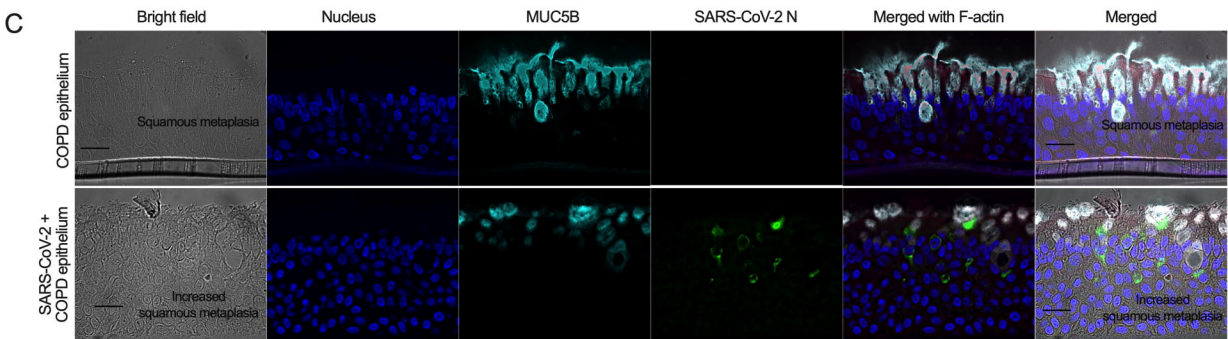
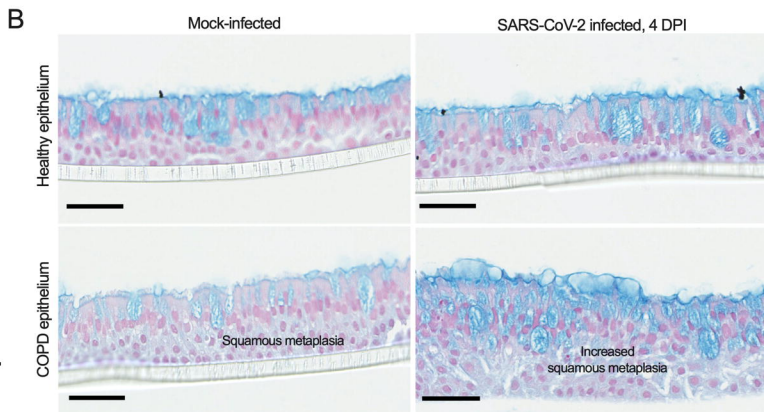
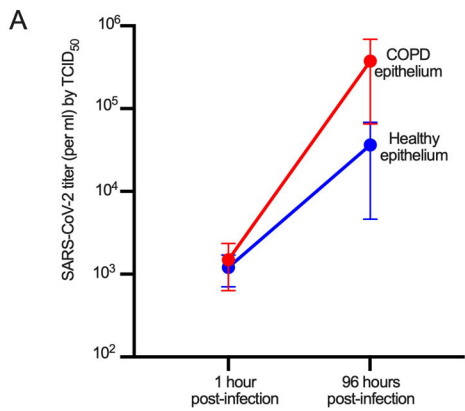


**Figure 6**

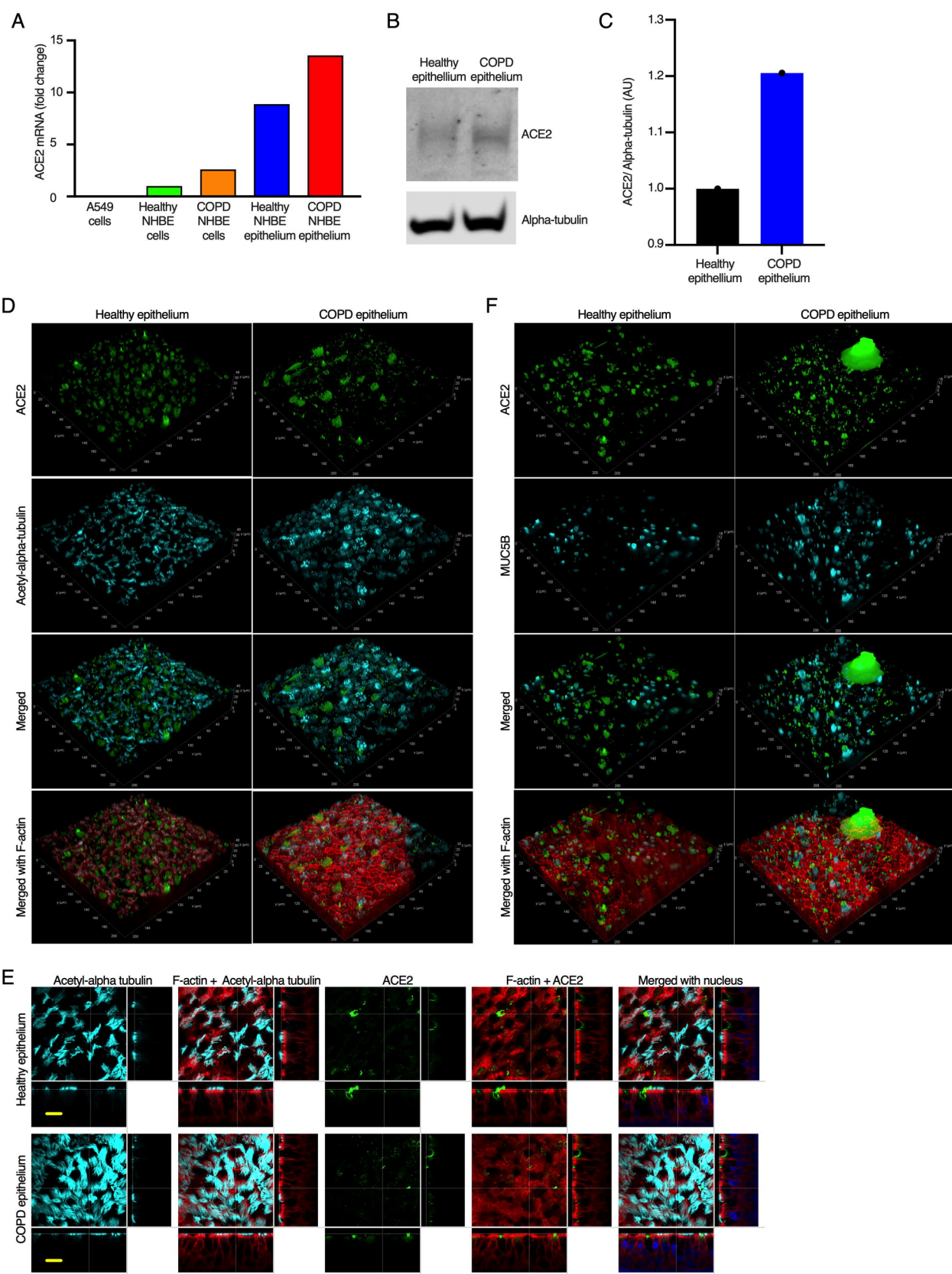


**Figure S1**

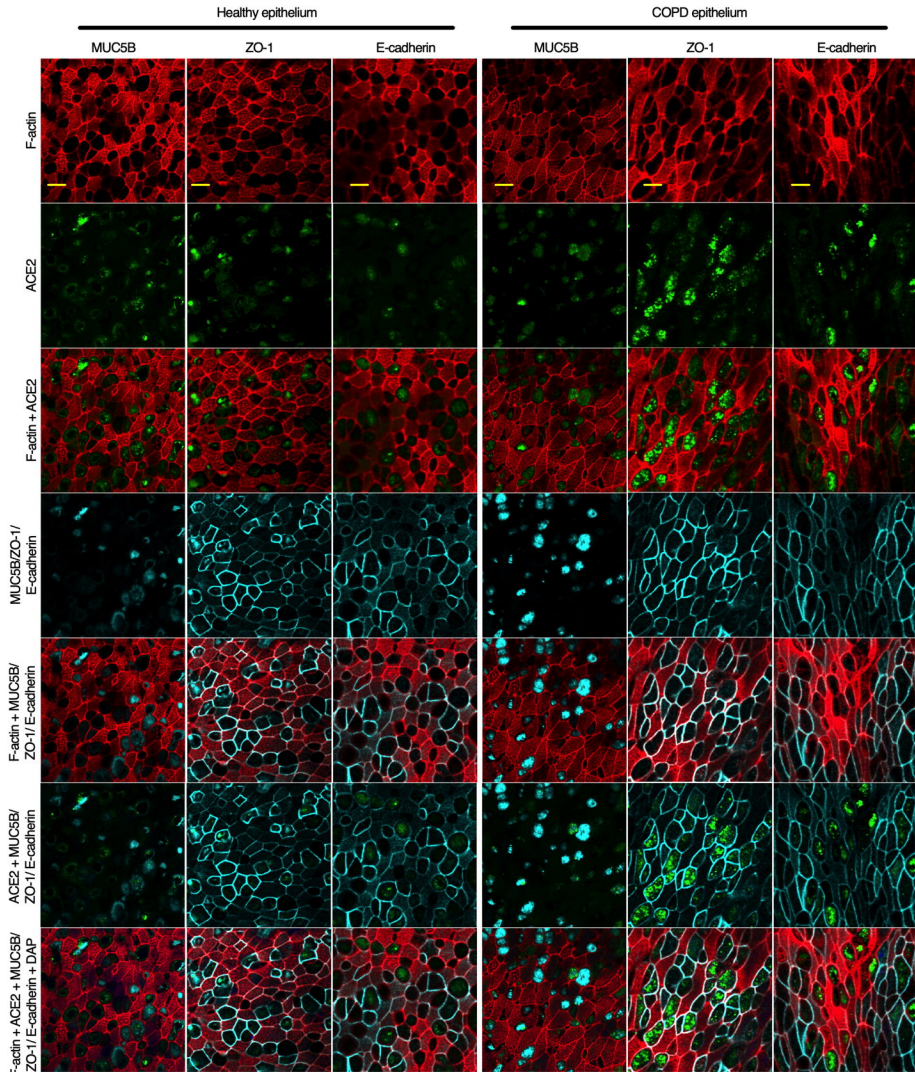


**Figure S2**

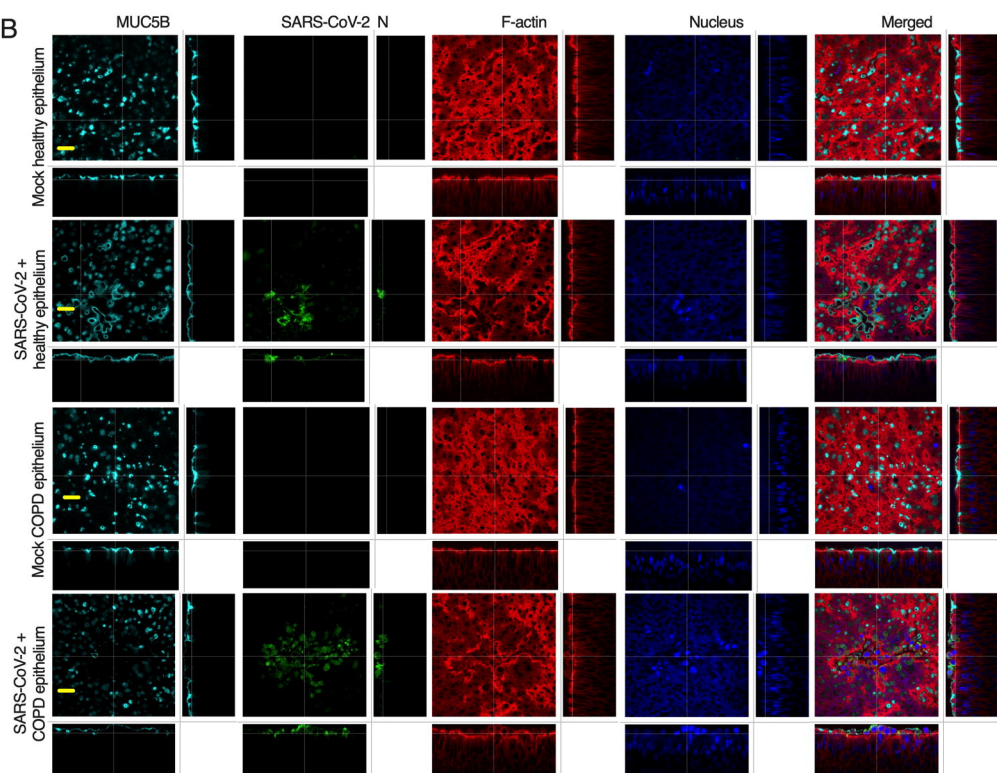
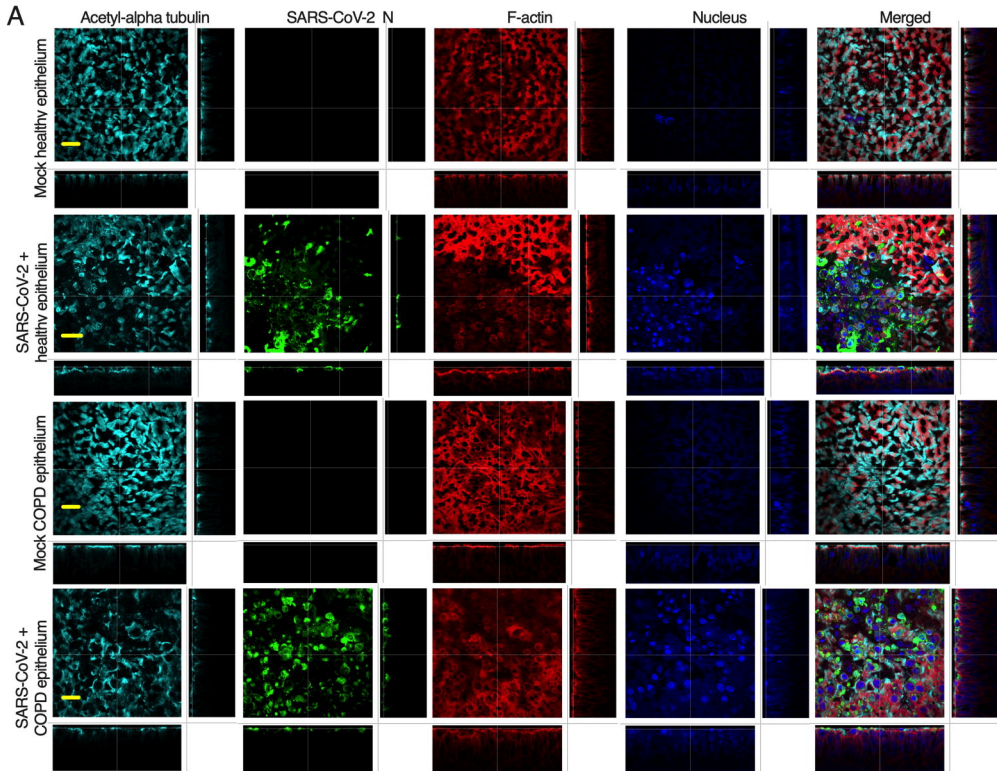


**Figure S3**

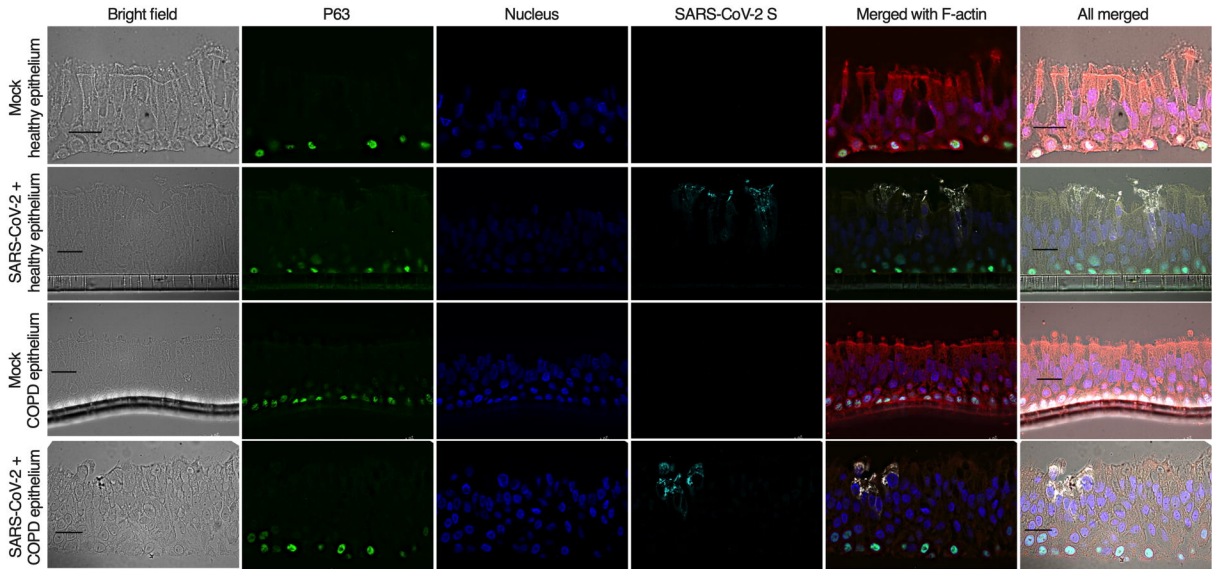


**Figure S4**

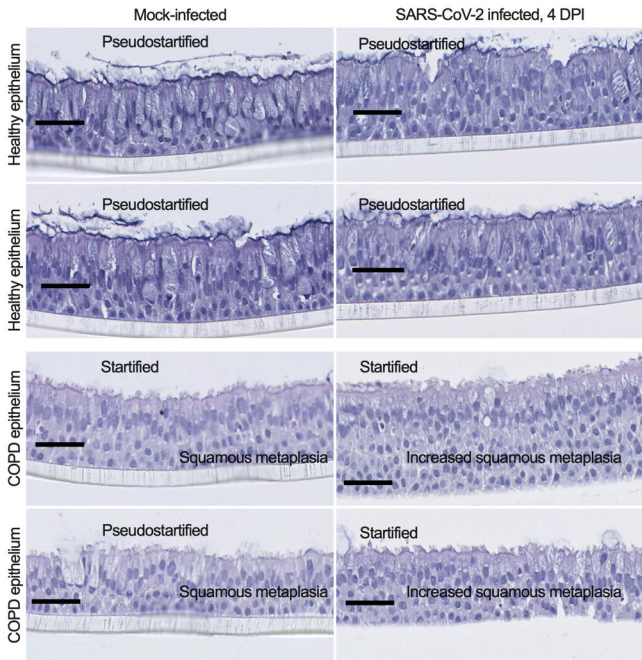
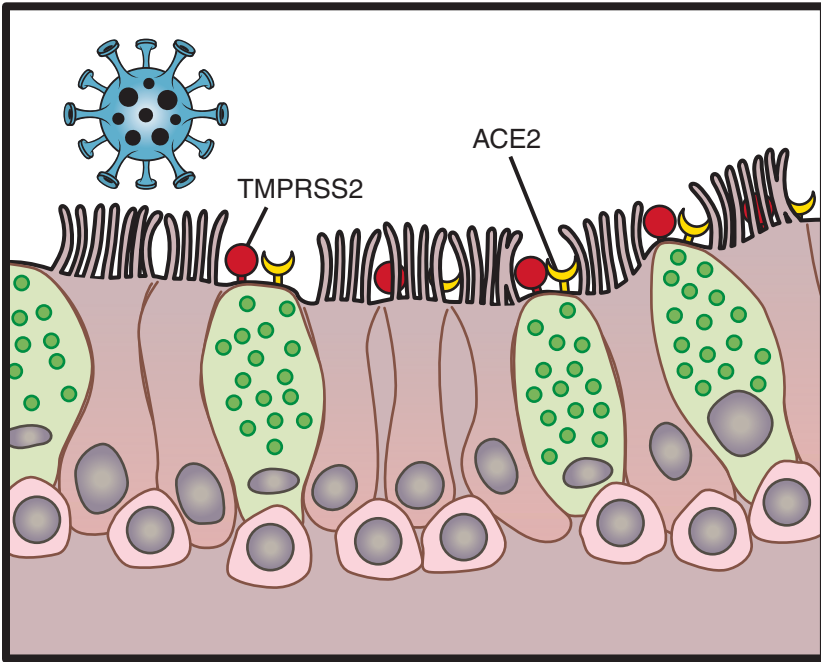


**Figure S5**

Healthy Epithelium



COPD Epithelium

